 doi:10.20944/preprints202205.0027.v1

Article

Reinforcement of Tooling Using Residual Stresses Generated by Cladding by Arc Welding

Rameez Israr [1,] *, Johannes Buhl [1], Sebastian Härtel [1] and Markus Bambach [2]

[1] Brandenburg University of Technology Cottbus–Senftenberg, Chair of Hybrid Manufacturing
[2] Advanced Manufacturing Lab, ETH Zurich, Leonhardstrasse 27, 8092 Zurich, Switzerland
* Correspondence: Rameez.Israr@b-tu.de

Abstract: Cladding is typically used to protect components from wear and corrosion while also improving the aesthetic value and reliability of the substrate. The cladding process induces significant residual stresses due to the temperature difference between the substrate and the clad layer. However, these residual stresses could be effectively utilized by modifying processes and geometrical parameters. This paper introduces a novel methodology for using the weld-cladding process as a cost-effective alternative to various existing reinforcement techniques. The numerical analyses are performed to maximize the reinforcement of a cylindrical tool. The investigation of how the weld cladding develops compressive stresses on the specimen in response to a change in the weld beads and the welding sequence is presented. For the benchmark shape, experimental verification of the numerical model is performed. The impact of the distance between the weld beads and the effect of the tool diameter is numerically investigated. Furthermore, the variation in compressive stresses due to temperature fluctuations during the extrusion process has been evaluated. The results showed that adequate compressive stresses are generated on the welded parts through the cladding process after cooling. Hence, the targeted reinforcement of the substrate can be achieved by optimizing the welding sequence and process parameters.

Keywords: Additive manufacturing (AM); Wire arc additive manufacturing (WAAM); Weld cladding; Residual stresses; Reinforcement; Hole drilling method; LS-Dyna; Numerical Simulation

1. Introduction

Reinforcements of metal components are used in various applications, e.g., increasing the strength of forming tools in regions where high loads need to be carried, reducing the degradation of components, enhancing the fatigue life, and minimizing distortions [1]. An extrusion tool is a typical application that requires reinforcements, as shown in Figure 1. The reinforcement enhances the tool life and erosion behavior of the tool and reduces elastic deformation.

1.1 Extrusion tool

Extrusion processes are known for their high dimensional accuracy and good surface quality [2]. The increased production rate makes this process cost-effective [3]. In metal extrusion, the forming forces are applied to one end of the tool, while the formed component is obtained either at the opposite end (forward extrusion) or the same end (reverse extrusion) [4]. In another form of extrusion known as double cup extrusion, the billet is squeezed into the desired shape between the two punches [5]. The movable upper punch is pushed towards the fixed lower punch, and the pressure is applied to the billet, which results in the free flow of the material around the two punches [5,6]. A double cup extrusion model is shown below in Figure 1.

 doi:10.20944/preprints202205.0027.v1

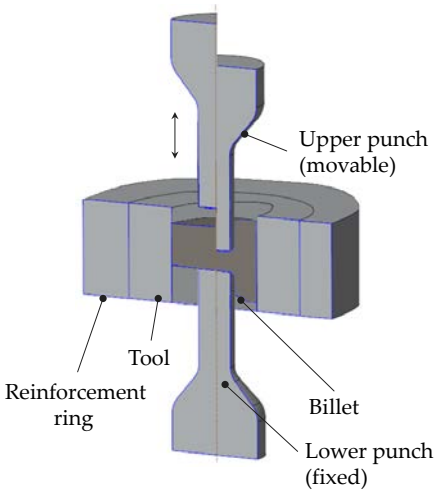

Figure 1. Schematic diagram of a double cup extrusion model.

As extrusion involves very high pressure, it causes the formation of high tensile stresses in the tool, which can lead to crack formation [7,8]. Tensile stresses develop on the inner side of the tool and limit its load capacity. A reinforcement ring (see Figure 1) is usually used around the tool to increase its strength. The reinforcement ring compensates for tensile stresses and provides the tool with additional strength [9]. Lange [10] reported that using a steel reinforcement ring around the extrusion tool raises the permissible internal pressure of the tool to 1390 MPa. Thus, by adding a single reinforcement ring around the tool, the internal pressure-bearing capacity of the tool can be increased up to 80 % relative to the tool without a reinforcement ring. Klocke et al. [9] stated that extrusion dies without reinforcement rings lose 37.5 % of their strength during extrusion. Placing two reinforcement rings next to each other enhances the internal pressure bearing capacity of the extrusion tool by 27 % [9]. Therefore, to increase the strength of the extrusion tools, either the undesired tensile stresses should be minimized or reinforcement should be applied [11].

1.2. Reinforcement of toolings

Numerous metal components are reinforced by applying external pressure on them by various techniques. The press-fit or thermal shrink-fit method has been used to generate compressive stresses on the cylindrical components to reinforce them [11].

A commonly used industrial approach for reinforcing a cylindrical rod using the shrinkage of a hot ring is presented in Figure 2. In this process, the metal ring is heated to a defined temperature, such as 1000 °C [12], followed by mounting on the cylindrical rod and left to cool. The heating causes the thermal expansion of the metal ring and its diameter increases. When the ring cools off, the thermal contraction of the metal develops compressive stresses on the rod due to the close fit between the rod and the ring. These compressive stresses increase the strength and enhance the fatigue life of the metal rod [13].

 doi:10.20944/preprints202205.0027.v1

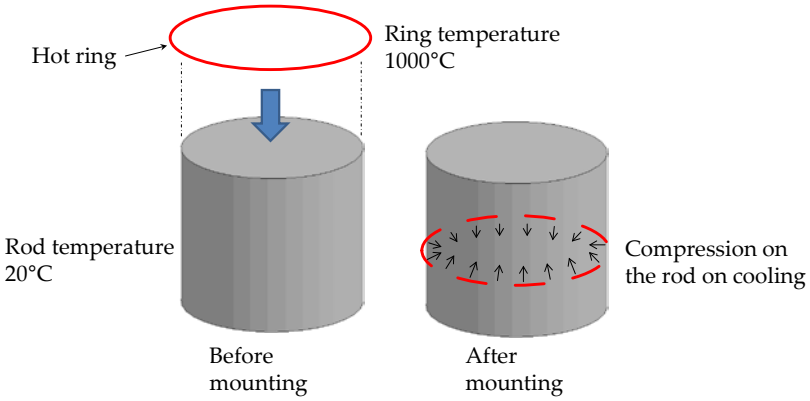

Figure 2. A conventional method of reinforcing a metal rod using the shrinkage of a metal ring.

The method mentioned above for reinforcing the components is very effective and cheap, but it has some disadvantages. Since it requires a tight tolerance between the shaft and the bore (interference fit P7/h6 [14] according to ANSI B4.2 [15]), positioning of the hot ring must be done with advanced tools, such as hydraulic presses, mounting levers and mounting clamps [16].

Although shrink fitting is used to enhance the fatigue life of the components [17], the most significant disadvantage of shrink fitting is that it can only be used on cylindrical components [18]. On the other hand, the hot ring can damage the rod if it dislocates from its axis or if the compressive stresses applied to the ring increase the tensile strength [19]. This method could also significantly change the stress and strain profile and generate considerable tensile stresses on the surface [20]. It may initiate cracks that could propagate and eventually lead to specimen failure [11,21]. Shrink-fit requires exact fittings between the adjacent surfaces, leading to complications when dealing with larger components [17].

In addition, to shrink fitting, other techniques, such as thermal autofrettage, mechanical autofrettage, explosives, and part rotation can reinforce the components. The autofrettage process generates a very high pressure within the tube cavity, inducing compressive residual stresses after the pressure is released [22]. According to Thumser et al. [23], the thermal autofrettage of a round, symmetrical part increases its endurance limit and reduces the amount of tensile residual stresses, particularly from the internal surface. Jahromi et al. [24] claimed that the autofrettage of a metal tube with reinforced ceramic particles on its inner surface increases the amount of compressive residual stress. Shufen et al. [25] proposed that locally heating a 1080-steel tube to an elevated temperature using thermal autofrettage followed by its cooling induces compressive stresses at its inner surface. They reported that the development of the compressive residual stresses during cooling increases the fatigue performance of the tube. Kamal et al. [26] imposed high pressure on the inner surface of an SS304 steel tube using thermal autofrettage, which after cooling, developed compressive residual stresses on its surface. They found that the load-carrying capacity and the fatigue strength of the tube enhanced due to compressive stresses. Besides thermal autofrettage, Malik et el. [27] used a mechanical autofrettage method to compress a thick steel cylinder using a conical mandrel. This method develops compressive stresses in the cylinder and strengthens it. Kaplan et al. [28] used an explosive method to reinforce the thick-walled forging dies made of steel and aluminium. They used high-pressure explosive energy in a controlled way to establish plastic flow on the surface of the die-cavity. With the reduction of the pressure from the die, high residual stresses are generated. Zare et al. [29] utilized a rotational method to strengthen a thick-walled cylinder. They rotated the cylinder with a high angular velocity, which developed compressive residual stresses and resulted in its reinforcement. Although the procedure mentioned above offers reinforcement, they primarily create compressive stresses on the internal cavity of the cylindrical specimen. They may also significantly increase the harmful tensile stresses on the cylinder's exterior surface, leading to cracking [30].

 doi:10.20944/preprints202205.0027.v1

Some other conventional methods to strengthen the components include grain boundary strengthening [31], solid solution strengthening [32], heat treatment [33], precipitation hardening [34], and cold working [35]. Apart from these conventional surface hardening techniques, weld cladding, in which a metal is welded/coated with a layer of another or same metal, is also an effective method to minimize the tensile residual stresses, hence, improving the mechanical properties of components (up to 3 mm or more) [36]. In the past, various metals have been used as a coating/clad to achieve the desired properties, i.e., nickel, steel alloys, copper alloys, manganese alloys, and composites [37]. Since it is known that welding causes residual stresses, various researchers have sought to minimize the stresses by weld cladding. Pan et al. [38] coated the high strength steel grade 16Mn on the surface of steel grade 9Cr to enhance the hardness and reduce the residual stresses and corresponding wear and crack propagation. Jiang et al. [39] reported that high thermal loads during cladding create tensile stresses, which might cause cracks and weaken the material. They suggested increasing the number of clad layers on the metal surface for reducing tensile residual stresses. However, they did not mention the optimized number of layers and their pattern. Benghalia et al. [40] used the weld-cladding process on a cylindrical substrate to strengthen it. They revealed that weld-cladding develops more compressive stresses on the substrate than the typical shrink-fit joint. The compression reduces the pre-existing tensile residual stresses on the substrate and enhances the compressive stresses, increasing its strength.

Numerical techniques are becoming an essential tool for estimating temperature, distortion, and residual stresses caused by the welding processes. Several simulation techniques have been presented to compute the thermal behavior during the cladding process in recent years. Weld-cladding simulations are typically performed by thermo-mechanical simulation methods, which predict the global thermo-mechanical behavior of the weld. Incorporating thermal material parameters into the model at the melting point and room temperature simplifies this behavior [41]. Lou et al. [42] developed a three-dimensional finite element model to examine the influence of a heat source on a heat-affected zone. They also observed the effect of cooling rate on the cladding layer. Gao et al. [43] developed a 3D thermal FEM model to simulate the temperature field in the Fe-based weld cladding. They evaluated different process parameters, i.e., temperature distributions, cooling rate, and solidification rate. Kumar et al. [44] developed a 3D model to estimate various physical phenomena, i.e., heat transfer, fluid flow, and convection during the cladding process. They observed that changing the scanning speed changes the area of the weld pool and the degree of convection. Smith et al. [45] evaluated the welding of a single clad layer using more than 40 finite element simulations to assess the influence of different process variables on the expected residual stresses. They observed that the hardening modulus of the material has a significant impact on the developed stresses. However, mesh size, welding efficiency, and thermal boundary conditions are less influential. Karlsson et al. [46] and Lindgren [47] analyzed the effect of different variables involved in the simulations on residual stresses, heat input, and deformation. They found that the material's heat capacity is one of the parameters that could affect the temperature distribution and resulting stresses. Feroozmehr et al. [48] utilized a finite element approach to investigate the influence of weld deposition patterns on the temperature and stress distribution during the cladding process. However, the weld bead dimensions and the deposition pattern that could generate the maximum compressive stresses on the specimen have not been explained.

From the state of the art, it can be concluded that various methods have been used to enhance the strength of the components by cladding. However, no previous study could be found in which weld cladding induced targeted residual stresses in a tool. Moreover, there is no information on how multiple clad layers should be welded to maximize the compressive stresses on the component's surface, where operating stresses are usually the highest. Topics requiring further investigation include: the effect of the number of clad layers, the number of beads in a layer, size of the beads, the distance between the different

 doi:10.20944/preprints202205.0027.v1

layers, and the effect of cavities on the developed stresses. In the present study, weld cladding is introduced to induce compressive stresses in a cylindrical tool in a controlled manner.

1.3. Scope and structure

The main goals of the present research are:

- to utilize stresses of the weld-cladding process for reinforcing the cylindrical tool,
- to adopt the weld-cladding pattern to maximize the compressive stresses on a cylindrical tool surface,
- to find how the weld-bead size affects the compressive stresses on the tool,
- to analyze the effect of changing the tool's materials and process parameters on the maximum achievable compressive stresses.

The paper is structured as follows. Section 2 explains the materials and methods. In subsection 2.4, the simulation model is introduced. Section 2.1 presents the experimental procedure, i.e., specimen production, welding preparation, and residual-stress measurement technique. In section 3, the results of a single bead numerical model are validated with the experiments to prove the accuracy of the numerical model, followed by the detailed evaluation of different modeling strategies and process parameters using the numerical analysis. Finally, section 4 reports the summary and conclusions drawn from this work.

2. **Materials and Methods**

2.1. Numerical procedure

A three-dimensional Finite Element FE model of the demonstrator shape was developed to study the thermal history and residual stresses and optimize the welding parameters and trajectories for single and multiple weld beads. The effect of multiple beads in single and multiple layers is investigated. Different weld-bead materials and their influence on generating the compressive stresses are tested using a single bead model. After validating the simulation results with experiments, various welding paths and bead sizes were modeled and analyzed to understand the development of compressive stresses on the tool's surface after cooling.

2.1.1. Material model

The thermal analysis was carried out using the material model **`*MAT_Thermal_CWM T07`**. It is a material definition with temperature-dependent properties in which the materials are created or activated depending on temperature. The thermo-elastic plastic material **`*MAT_CWM 270`** with kinematic hardening and the von Mises yield criterion were used for the structural analysis. The thermo-mechanical material properties of steel grade 309L correspond to the steel used in the experiments. Details of the material parameters and properties of steel 309L can be found in the earlier work of Israr et al. [49]. The thermo-mechanical properties of some other materials are given in Table 1.

Table 1. Thermo-mechanical parameters of different materials at room temperature

Material	Coefficient of expansion α (10^{-5} °C^{-1})	Heat capacity C_P(10^6 mJ/Ton °C)	Brinell hardness HB	Yield strength $Rp_{0.2}$ (MPa)	Thermal conductivity k (W/m °C)	Melting Temperature T (°C)
Titanium [50–52]	0.80	610	334	830	5.8	1655
Inconel 718 [53,54]	1.30	435	201	758	11.4	1336
SS304L [55,56]	1.66	462	147	230	14.6	1400
S235 [57,58]	1.61	480	120	235	13	1420
A36 [59,60]	1.65	481	119	250	20	1426
TZM [61,62]	0.52	305	225	842	118	2623

Preprints (www.preprints.org) | NOT PEER-REVIEWED | Posted: 5 May 2022 doi:10.20944/preprints202205.0027.v1

SS309L [55,63]	1.65	500	160	400	20	1454
Maraging steel MS1[64]	1.70	446	353	1800	14.6	1413

2.1.2. Element activation technique

The beads (filler metal) deposition on the substrate (tool) was carried out using ghost material properties, i.e., the quiet element technique. In this technique, all the elements of weld beads are kept quiet/inactivated at first. The inactive elements of the beads remain in the model, but they do not affect the active beads. To prevent structural deformation below the melting point, inactive or dead elements are modeled with a deficient (factor of 0.1 or less of the properties at room temperature [65]) Poisson's ratio, young's modulus, and thermal expansion coefficient. At the same time, a very high value of heat capacity is set. The thermal material properties are activated first to ensure the addition of the material in structural analysis. The heat source activates the thermal properties of elements at a proper time step within a temperature range of 1200 °C – 1210 °C. In contrast, their mechanical properties are activated above the melting temperature, in the range of 1400 °C to 1450 °C for steel. A temperature range was used to activate both thermal and structural models to avoid convergence issues during the simulation.

A fully coupled thermo-mechanical implicit model having hexahedral solid elements with one-point integration and viscous hourglass control was used for the structural analysis. All simulations were performed with a double-precision solver (ls-dyna_smp_d_R11) in LS-DYNA.

A tied (mechanical) contact was established between the beads from the start of the simulation. In contrast, the time-dependent thermal contacts were enabled between the neighboring beads at a pre-defined time. The boundary conditions for convection and radiation on the tool and beads were associated with the initiation of thermal contact between the connected surfaces. Heat loss via convection and radiation begins from the exposed surfaces of the active beads.

2.1.3. Heat source model

The basic concept of a heat source is to model an isothermal surface of the weld pool, where the heat flow is quite near to reality [66]. In this work, Goldak's double ellipsoid heat source model is used for thermal analysis, as presented by Goldak et al. [67]. The following equations determine the power density distribution in the front and rear regions:

$$q_f(x,y,z,t) = \frac{6\sqrt{3}f_f Q}{\pi\sqrt{\pi}abc_f} e^{-3\left(\frac{x}{a}\right)^2} e^{-3\left(\frac{y}{b}\right)^2} e^{-3\left(\frac{z+v(\tau-t)}{c_f}\right)^2} \quad (1)$$

$$q_r(x,y,z,t) = \frac{6\sqrt{3}f_r Q}{\pi\sqrt{\pi}abc_r} e^{-3\left(\frac{x}{a}\right)^2} e^{-3\left(\frac{y}{b}\right)^2} e^{-3\left(\frac{z+v(\tau-t)}{c_r}\right)^2} \quad (2)$$

The sum of the forward and rear heat fractions should equal 2.

$$f_f + f_r = 2 \quad (3)$$

The total heat introduced in the model by the heat source and the total heat loss due to conduction, convection, and radiation is given by:

$$q_{Total} = q_{input} - q_{lost}$$
$$q_{lost} = q_{conduction} + q_{convection} + q_{radiation} \quad (4)$$

Preprints (www.preprints.org) | NOT PEER-REVIEWED | Posted: 5 May 2022 doi:10.20944/preprints202205.0027.v1

Table 2 presents the various parameters of Goldak's heat source used in this study. The parameters n = 1, v = 7.5 mm/s, and f = 1 remain constant for all the models, while the remaining heat source parameters are changed according to the bead shapes, as explained in previous work [49,68].

Table 2. Goldak's ellipsoidal heat source parameters for different dimension beads

Parameter	Symbol	A1	A2	A3	A4
Weld pool width	a	2.25 mm	2.5 mm	3.0 mm	3.75 mm
Weld pool depth	b	3.0 mm	3.3 mm	4.0 mm	5.0 mm
Weld pool (forward direction)	c_f	1.5 mm	1.6 mm	2.0 mm	2.5 mm
Weld pool (rear direction)	c_r	6.0 mm	6.4 mm	8.0 mm	10.0 mm
Weld pool energy	Q	1840 W	2248 W	3271 W	5111 W

The welding parameters for all simulations were kept the same. The weld pool energy was adjusted according to the weld-bead geometry by maintaining a constant welding-energy to bead area ratio.

2.1.4. Meshing and clamping

The tool was fixed at its bottom (represented by the yellow marks in Figure 3). Only the lower nodes were fixed set, allowing the tool to contract and expand freely under the thermal loads, as in the experiments. The welding time for a single bead on the tool was approximately 46 s, with a welding velocity of 7.5 mm/s. A complete welding cycle was divided into 90-time steps of 0.5 s each. Considering higher temperatures and heat flows along the z-axis, the mesh size in the welding zone was set to 0.5 mm, whereas a coarser mesh size of 2 mm was used outside the welding zone. The mesh size in the circumferential direction was kept constant at 10.45 mm, as shown in Figure 3.

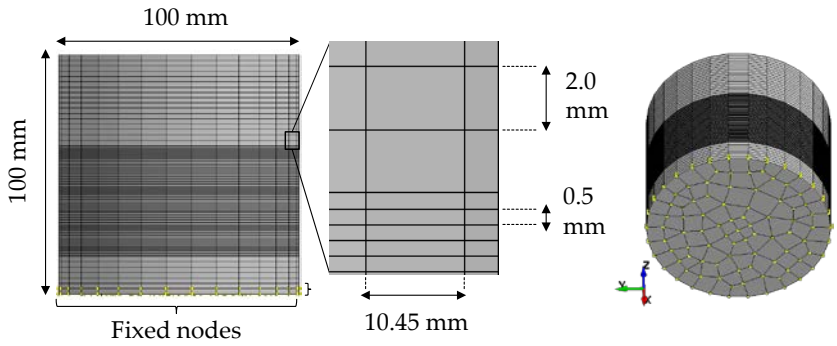

Figure 3. Dimensions, mesh-size, and position of the fixed nodes of the tool (cylinder)

2.2. Finite Element Model (FEM) of a Single-bead cladding

The finite element model of a single bead of various cross-sections was constructed on a cylindrical tool (Figure 3). The beads were classified as A1-A4 according to their cross-sections, as shown in Figure 4.

Preprints (www.preprints.org) | NOT PEER-REVIEWED | Posted: 5 May 2022 doi:10.20944/preprints202205.0027.v1

Tool (mm)	Bead A1(mm)	Bead A2(mm)	Bead A3(mm)	Bead A4(mm)
l = 100mm	d_i = 100	d_i = 100	d_i = 100	d_i = 100
d = 100mm	d_o = 106	d_o = 106.6	d_o = 108	d_o = 110
	w = 4.5	w = 5	w = 6	w = 7.5
	h = 3	h = 3.3	h = 4	h = 5

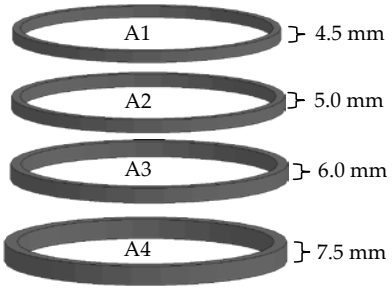

Figure 4. Dimensions of different beads for the reinforcement analysis.

Here, l and d are the length and the diameter of the tool, di and do are the inner and outer diameters of the beads, w is the width, and h is the height of the beads.

2.2.1. Weld-bead position on a tool with an internal cavity

Five numerical models with different bead positions were developed to investigate the influence of an internal feature, i.e., a cavity, in developing compressive stresses on the tool surface (see Figure 5).

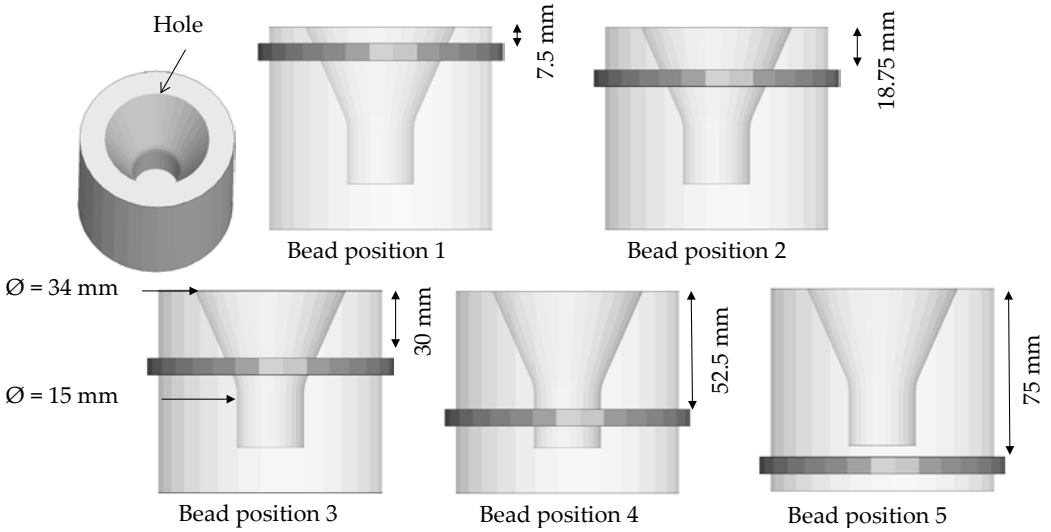

Figure 5. Welding a bead at different positions on the tool containing an internal conical hole.

The hole diameter at different positions can be seen in Figure 5. The dimensions of the bead and the tool remained constant in all models.

2.2.2. Welding on the tools of different diameters

Six different tool diameters, namely 40 mm, 45 mm, 50 mm, 55 mm, 60 mm, and 65 mm, were modeled to analyze the influence of the tool diameter on the reinforcement. The dimensions of tools and beads can be seen in Figure 6.

Preprints (www.preprints.org) | NOT PEER-REVIEWED | Posted: 5 May 2022 doi:10.20944/preprints202205.0027.v1

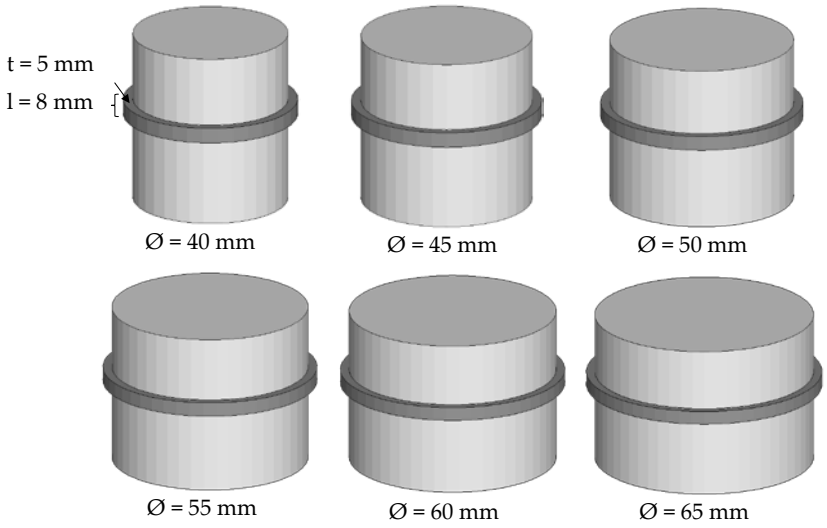

Figure 6. Tools and beads of different diameters while keeping a constant length and thickness of the beads.

The beads were designed with the same inner diameter as the tool's outer diameter, while the length and thickness of the beads were kept constant in all models.

2.3. Finite Element Model (FEM) for multiple-bead cladding

2.3.1. Single-layer parallel cladding of multiple beads with and without a gap

Models of two and five parallel weld beads in a single layer, with and without a gap, were built to assess whether weld beads parallel to each other influence the compressive stresses on the tool after cooling. Furthermore, the impact of introducing a gap between the beads and the resulting compressive stresses was also evaluated. The placement of 2 and 5 weld beads on the tool is depicted in Figure 7 (a)-(c). The welding is performed from the bottom to the top.

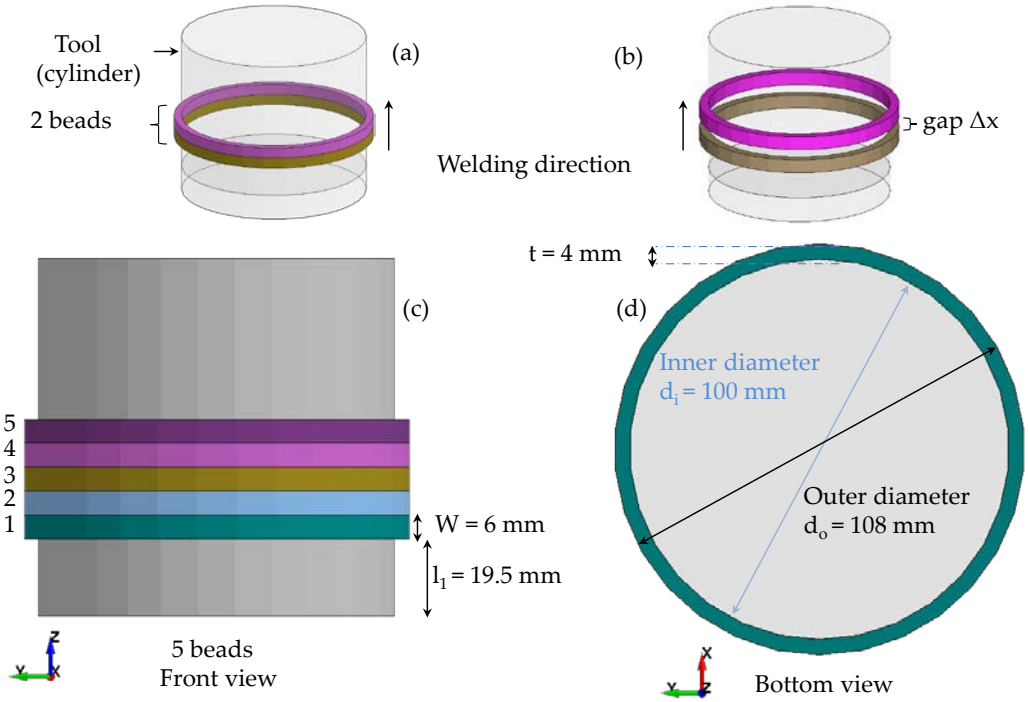

Figure 7. Patterns of two and five parallel beads without a gap (a), (c), two parallel beads with gap Δx (b), and dimensions of a bead welded on the tool (d).

Preprints (www.preprints.org) | NOT PEER-REVIEWED | Posted: 5 May 2022 doi:10.20944/preprints202205.0027.v1

The numbers on the left side of Figure 7 (c) represent the welding sequence, i.e., 1 to 5. The symbol l_1 describes the distance between the tool's base and the edge of the first bead. The remaining symbols are already explained in Figure 4.

2.3.2. Multilayer parallel welding of beads

The dimensions and positioning of the weld beads on the tool in multiple layered parallel welding are shown in Figure 8.

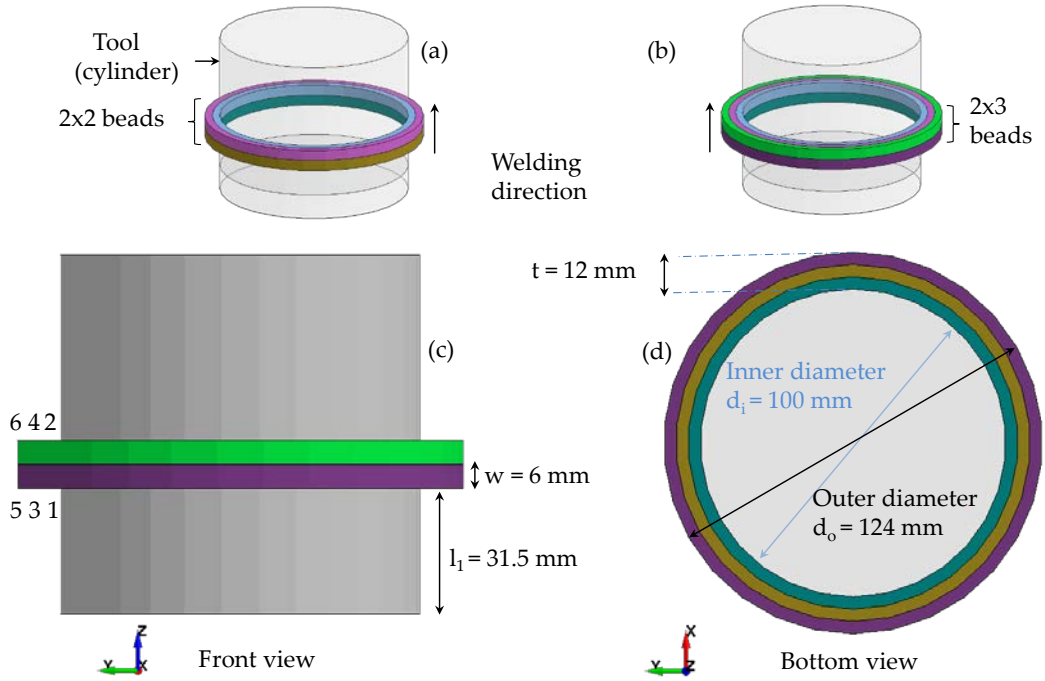

Figure 8. Pattern of the two beads in two layers (2x2) (a) and two beads in three layers (2x3) (b, c) on the tool with the A3 beads (d).

The numbers on the left side of Figure 8 (c) represent the welding sequence in three layers, i.e., 1 to 6. In Figure 8 (d), d_i represents the smallest diameter of the beads, while d_o denotes the diameter of the outer bead.

Various process parameters were used to categorize the global temperature development and the local temperature history of multilayer welding patterns. The time delay between the two consecutive weld beads might influence the global temperature development. Therefore, the effect of introducing a time delay in single and multiple layers was compared to models without a time delay. It is known that the temperature peaks will change when beads are welded in different trajectories [69]. Therefore, the welding direction was reversed to see how the resultant compressive stresses on the tool changes. Figure 9 shows the multilayer cladding models with different trajectories and process parameters, i.e., welding in the same direction and welding in the opposite direction.

Preprints (www.preprints.org) | NOT PEER-REVIEWED | Posted: 5 May 2022 doi:10.20944/preprints202205.0027.v1

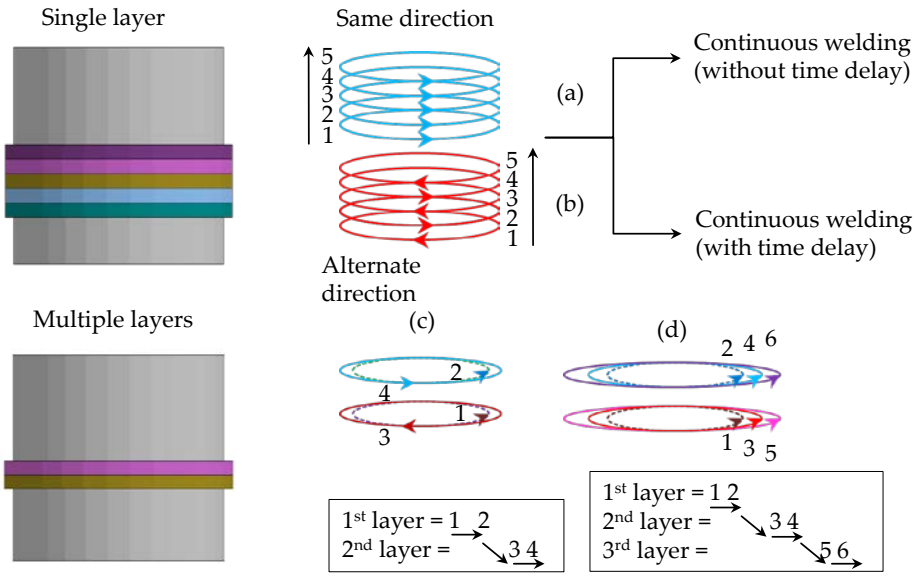

Figure 9. Welding trajectories for one-layer (a, b), two layers (c), and three layers (d) patterns.

Dotted inner circles in Figure 9 (c and d) represent the beads of the first layer, while the solid circles represent the beads of the second and third layers. The numbers above the arrows in Figure 9 (c and d) show the welding sequence, i.e., the two parallel beads were welded in the first layer, followed by the welding of the next two beads in the second layer.

Various welding trajectories of the 2x2 pattern can be seen in Figure 10.

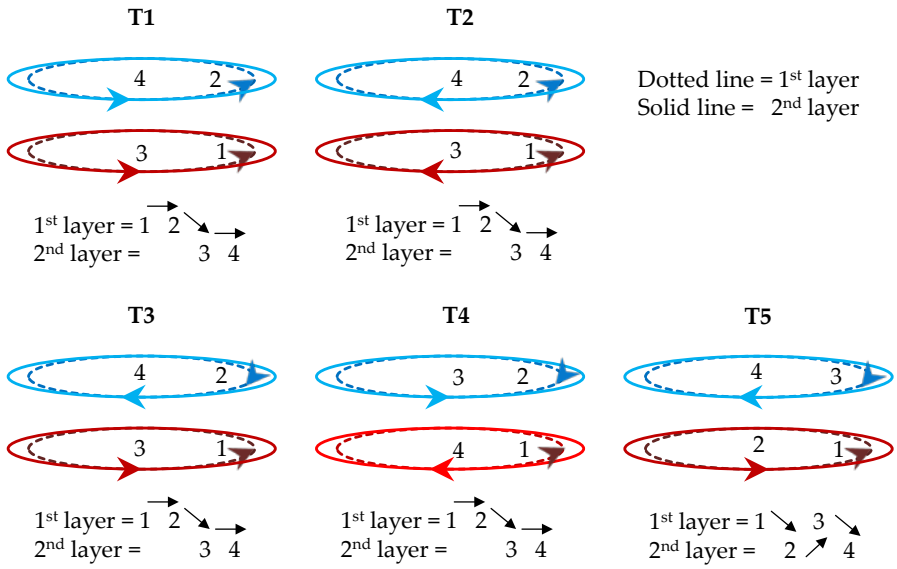

Figure 10. Comparison of various welding trajectories for 2x2 pattern.

The red and blue circles indicate the welding path, while the arrows represent the welding direction of the beads. Inner dotted circles represent the beads of the first layer, while the solid outer circles depict the beads of the second layer. The welding sequence of the beads in the two layers is indicated by the numbers above the circles and the path under each trajectory. For example, in trajectory T1, the first bead was welded in the first layer, followed by the second bead in the first layer. Then the third and fourth beads are welded in the second layer, and so on.

2.4. Experimental procedure for single-bead cladding

Preprints (www.preprints.org) | NOT PEER-REVIEWED | Posted: 5 May 2022 doi:10.20944/preprints202205.0027.v1

A solid cylinder having a length of 100 mm and a diameter of 100 mm was defined as a sample geometry. Since the experimental investigations were performed for validating the single-bead cladding simulation, the structural steel S-235JR was chosen as a tool material because of its good weldability and low cost. The experimental procedure was divided into two sections: the specimen's production and the measurement of the residual stresses.

2.4.1. Specimen production

The tests were carried out using a six-axis FANUC robotic arm with the parameters listed in Table 3.

Table 3. Welding parameters.

Parameter	Value
Welding current [I]	141 A
Welding voltage [U]	13.2 V
Torch travel speed [TS]	7.5 mm/s
Wire feed [WF]	123 mm/s

Solid welding wire ER70S-6 of 1.0 mm diameter was employed as a filler. Table 4 shows the chemical composition of the filler wire and the substrate according to American welding standards AWS [70] and Deutsches Institut für Normung DIN EN 10025-2 [71]. A shielding gas composed of 80 % Argon and 20 % CO_2 was used at a flow rate of 15.0 l/min to avoid oxidation and contamination of the weld pool [72].

Table 4. Chemical composition of S235 and ER70S-6.

	Element (Wt %)					
Material	**C**	**Mn**	**Si**	**P**	**S**	**Cr+Mo+Ni**
ER70 S-6	0.06 - 0.15	1.4 – 1.85	0.8 - 1.15	0.025	0.035 max	< 0.63
S235	0.17 max	1.40 max	-	0.045 max	0.045 max	-

The initial temperature of the specimen was 25 °C. The specimen's movement was limited during the welding process by clamping it at eight different positions, as shown in Figure 11.

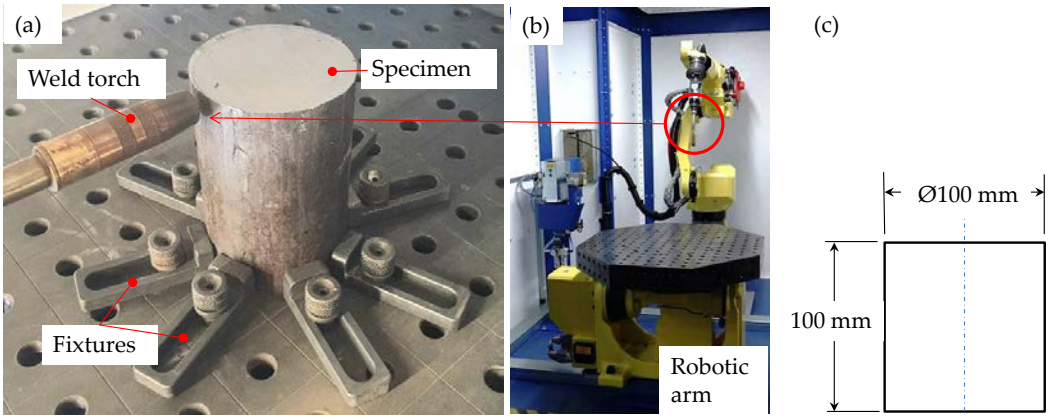

Figure 11. Arc welding setup with the mounted specimen (a), welding robot arm (b), and specimen geometry (c).

Beads were welded on the substrate using the parameters described in Table 3. During the welding process, the robotic arm with the attached welding torch positions vertical to the substrate. The machine-table starts rotating in a pre-defined path following an NC-code developed in Matlab and Rhino-3D, as explained by Nguyen et al. [73]. The welding time for a single bead was approximately 46 s, after which the tool was left to cool for the next 300 s without changing its position. A constant emissivity value of 0.9 was chosen

Preprints (www.preprints.org) | NOT PEER-REVIEWED | Posted: 5 May 2022 doi:10.20944/preprints202205.0027.v1

[74]. During welding and cooling processes, the temperature was captured using a thermal infrared camera (VarioCAM, Infratec) having an image resolution of 1.024 × 768 pixels at 1 frame/s. The height and thickness of the beads were 7.5 mm and 5 mm.

2.4.2. Residual stress measurement

In this work, the hole-drilling method, a semi-destructive method for measuring residual stress, was used to validate the simulation results. The hole-drilling method is fast, inexpensive, and can be used for a variety of materials. Although the hole drilling method does not always generate accurate results, the purpose of using this method is to get a rough estimate of the stress distribution by having some qualitative statements without a detailed analysis.

During the drilling procedure, few residual stresses are relieved, and comparable strains on the surface of the specimen are evaluated using the strain gauges. The three strain gauges (also known as rosette strain gauges) are attached to the surface of the specimen to determine the strains around the drilled holes (see Figure 12 (a)). Based on the strains, residual stresses are calculated using the calibration constants. For the stress analysis, a disc-shaped specimen was cut-off from the middle of the weld bead along section A-A. A hole-drilling method along with the position P of the hole in the specimen is shown in Figure 12.

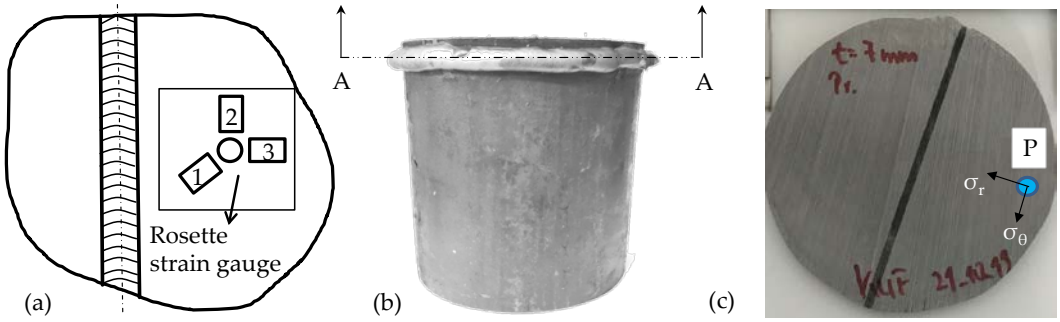

Figure 12. Schematic representation of the hole drilling method (a) according to [23], cut section (A-A) of the tool to measure the residual stresses (b), and the location of the drilled hole P on the cut section (c).

3. **Results and discussions**

3.1. Single bead weld-cladding simulation

The heat source melts the metal wire during the welding process and builds up a bead. The molten metal causes thermal expansion of the material on the surface of the substrate. On cooling, the shrinkage of the metal develops stress on the weld bead and the substrate material near the weld, as shown in Figure 13. After cooling, the thermal expansion creates more visible stresses on the tool's surface. Increasing compressive stresses on the tool surface are governed by the thermal loads and the shrinkage of the weld beads during solidification. Temperature and radial stress development in the numerical model of the demonstrator is shown in Figure 13.

Preprints (www.preprints.org) | NOT PEER-REVIEWED | Posted: 5 May 2022 doi:10.20944/preprints202205.0027.v1

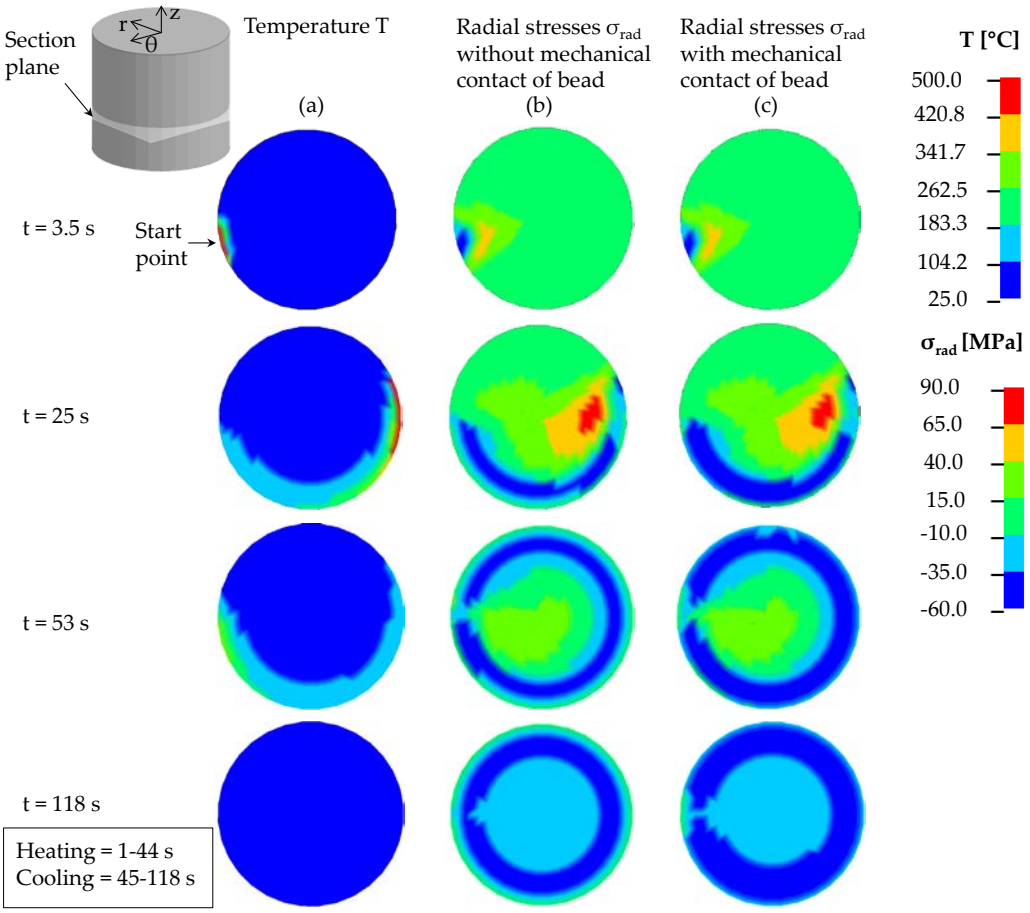

Figure 13. Temperature (a) and radial stress development on the tool (along a section plane) without mechanical contact of the bead (b) and with mechanical contact of the bead (c) at different times.

The temperature development can be seen along the cross-section in Figure 13 (a), while Figure 13 (b-c) shows the radial stresses in the tool. The thermal loads without any influence of the bead are demonstrated in Figure 13 (b). Figure 13 (c) shows both thermal and mechanical stresses from the weld bead. Most of the stresses in the tool arise from thermal loads during welding, as can be seen in Figure 13 (b). During welding, at time t = 3.5 s (start of welding), compressive residual stresses are generated in the heat-affected area of the tool, surrounded by tensile residual stresses, as can be seen in Figure 13 (b) and Figure 13 (c). When the heat source moves away, cooling begins on the tool's surface. Due to the shrinkage of the weld bead, the compressive stresses are generated on the outer surface of the tool (see Figure 13 (c)). Due to the thermal shrinkage of the material at t = 53 s (at the end of the welding phase), the tensile stresses in the middle of the tool decrease due to global cooling, and the compressive stresses dominate (see Figure 13 (b), Figure 13 (c)). After the sample has cooled to room temperature (at 118 s), the compressive residual stresses dominate, except in the start/stop region. The mechanical contact of the beads with the tool generated approximately 40 - 60% of the internal stresses, while the thermal loads caused the rest. Therefore, it can be concluded that the combined compressive stresses of thermal loads and the shrinkage of the weld bead build up compressive stresses and strengthen the tool.

The mean surface temperature and the equivalent stress for an element (having a size of 10.45 mm x 0.5 mm) are shown in Figure 14. As the heat source moves away from the reference element, the liquid metal solidifies, causing thermal shrinkage, visible in the sloping curve. After cooling to around 70 °C, the stress curve reveals a constant value of approximately 160 MPa on the tool surface.

Preprints (www.preprints.org) | NOT PEER-REVIEWED | Posted: 5 May 2022 doi:10.20944/preprints202205.0027.v1

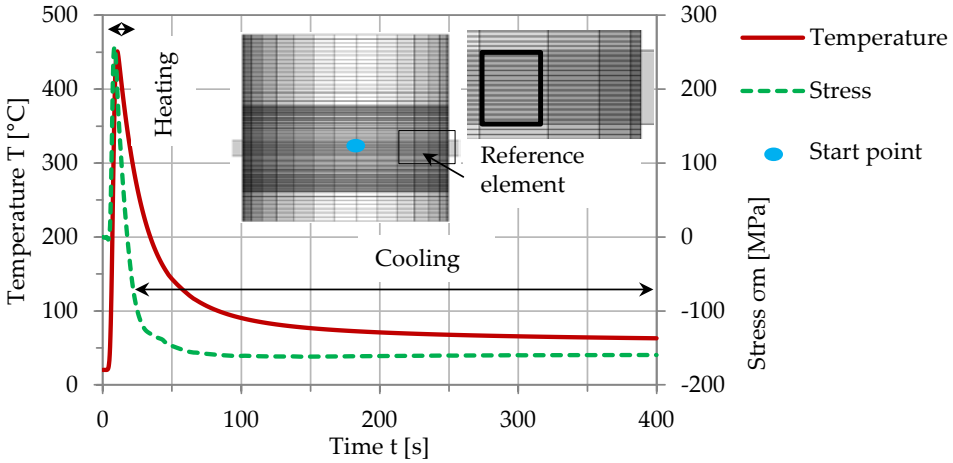

Figure 14. Stress and the temperature history on the tool surface in typical weld-cladding simulation (A4 bead).

3.2. Experimental validation of single bead simulation

The temperature distribution was recorded, and the outcomes were compared at different instances, i.e., at the beginning of the welding (0°), after welding half bead (180°), and after the complete bead (360°), as shown in Figure 15.

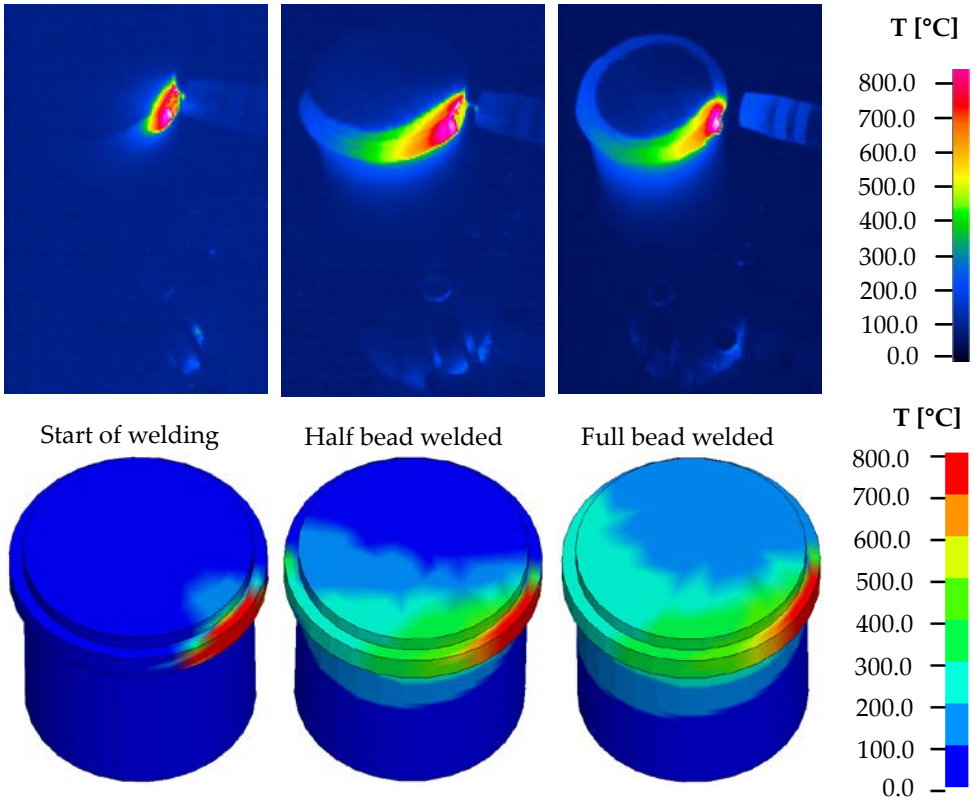

Figure 15. Temperature distribution pattern in the experiment (above) and simulation (below).

Results indicated that the temperature development in both the experiment and the simulation followed the same trend. The heat distribution pattern on the tool's surface can also estimate the welding path. The thermal history of two points at different locations on the tool has been compared, as shown in Figure 16. Temperature peaks indicate the moment when the heat source moves over the element. As point P1 was close to the welding bead, a higher peak was detected than P2, relatively far from the welding bead.

Preprints (www.preprints.org) | NOT PEER-REVIEWED | Posted: 5 May 2022 doi:10.20944/preprints202205.0027.v1

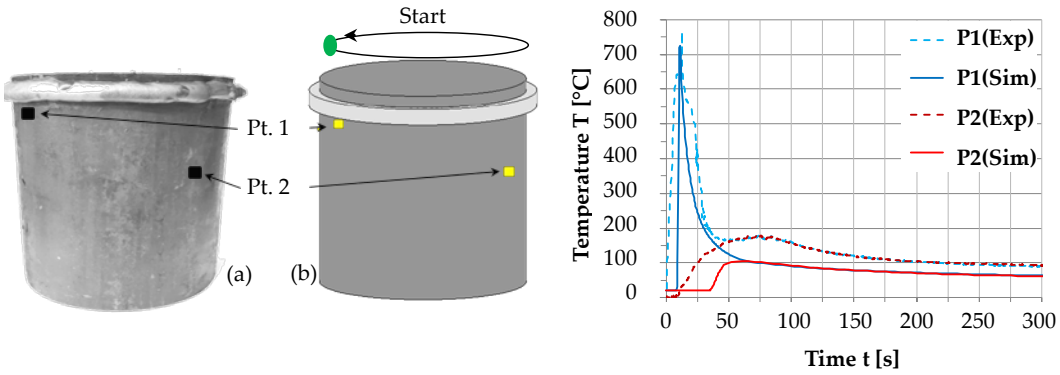

Figure 16. Thermal history of different points on the tool in the experiment (a) and the simulation (b).

After cooling, a 7 mm disk-shaped specimen was cut out of the tool with a metal-cutting saw and finished for stress measurement using a hole-drilling machine PROTEC. A hole diameter of 1.7 mm and a hole depth of 0.6 mm were achieved during the drilling, as detailed in section 2.3.2. The residual stresses along the radial and theta directions were measured at point P of the specimen (see Figure 17).

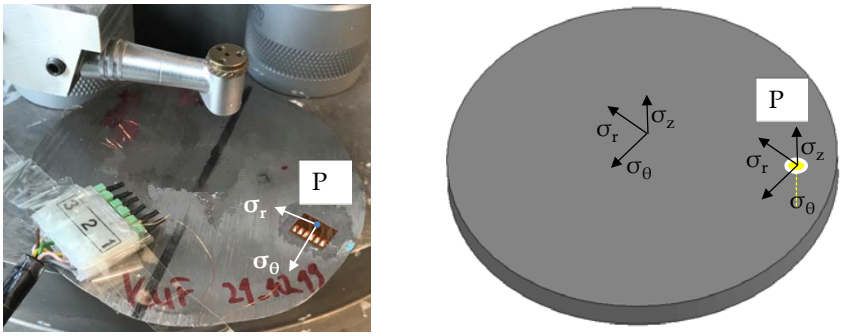

(a) Stress measurement with hole drilling apparatus

(b) Stress measurement in simulation along the depth

Figure 17. Position of the residual stress measurement point in hole drilling experiment (a) and numerical analysis (b).

A comparison of experimental and simulation results for radial and theta stresses along point P is presented in Figure 18.

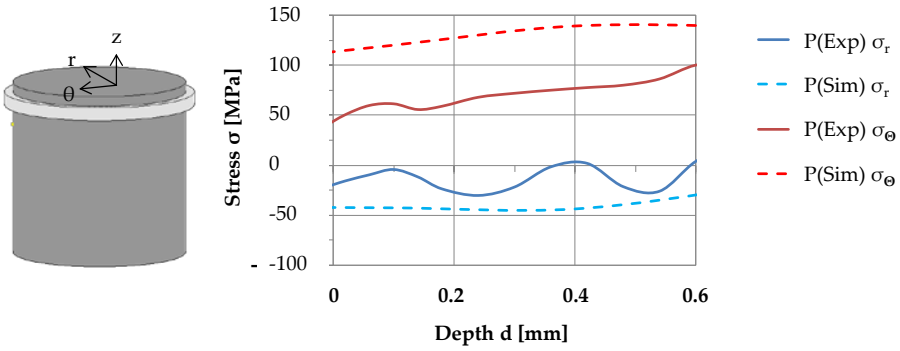

Figure 18. Residual stress history along the hole-depth at point P in the experiment and simulation.

The radial stresses σ_r in the tool along point P were mainly compressive, while the stresses in theta direction σ_θ were tensile (see Figure 18). After the tool cooled, more compressive stresses were observed, which caused the reinforcement of the tool.

Preprints (www.preprints.org) | NOT PEER-REVIEWED | Posted: 5 May 2022 doi:10.20944/preprints202205.0027.v1

For further analysis, only the simulation of the various geometric models will be performed, and results will be presented. In the post-simulation analysis of LS-Dyna, the pressure exerted on the tool's surface by the molten metal is assumed to be equivalent to mean stress [75], so in the following text, the mean stress σ_m on a particular element of the tool will approximate the reinforcement. After the part has cooled to room temperature, the stress history of the specified elements will be compared to analyze the results.

3.3. Optimization of a single-layer, multiple-beads cladding

More than one bead is welded parallel to each other in a layer to observe their influence on each other and the resulting stresses they induce on the tool surface. It should be noted that the multiple beads are welded continuously without giving a pause time to cool the previous bead to room temperature. The effect of adding pause time between the beads will be presented in the following section.

3.3.1. Influence of the numbers of beads and their dimensions

The number of beads and their cross-section could affect the stress distribution on the tool surface, as also demonstrated by Jousten et al. [76]. Figure 19 compares the stress histories of 2-beads and 5-beads models of different dimensions.

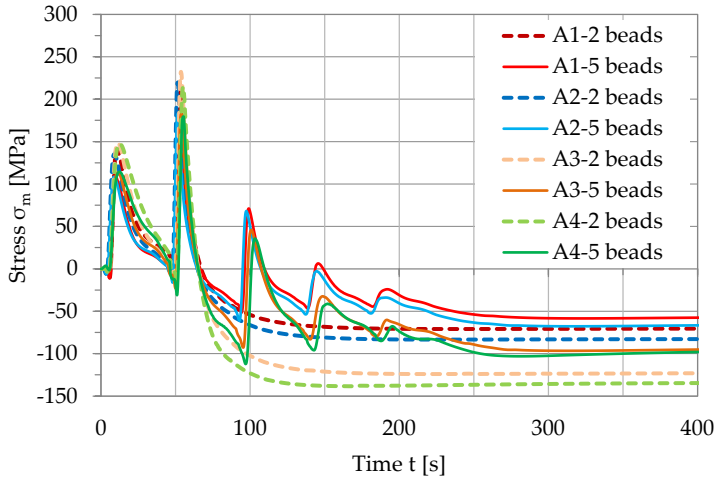

Figure 19. Comparison of the stress history of the tool element with two and five parallel weld-beads of different dimensions (A1-A4).

The position of the referenced element on the tool surface is highlighted in yellow. The FEA models have been developed for two and five parallel weld beads of various sizes, namely A1, A2, A3, and A4 (see Figure 4). Here the welding direction is from the bottom to the top, i.e., the bead at the bottom is welded first, followed by the bead at the top. It can be seen that as the heat source gets closer to the referred point, which is on the top bead, the material expands, and tension develops on the elements underneath the beads. As the referenced element lies under the top bead, a higher stress peak was observed when the heat source passed over it, as shown in Figure 19. The beads solidified and shrank as the temperature dropped, revealing the compressive stresses on the tool surface.

The compressive stresses experienced by the tool also vary with the size of the beads. Smaller beads, such as A1 and A2, induced less compressive stresses on the tool. The compressive stresses on the tool enhanced as the beads became larger. More heat flow between the beads and the tool has been observed in bigger beads A3 and A4. As a result of the increased heat transfer, more thermal expansion and shrinkage were counteracted by the colder material around it, resulting in more compressive stresses, which produced more compressive stresses on the tool [77].

The difference in the stress histories of the 2 and 5 beads models can also be seen in Figure 19. Compared to the 2-beads model, the 5-beads model introduces more heat into the

Preprints (www.preprints.org) | NOT PEER-REVIEWED | Posted: 5 May 2022 doi:10.20944/preprints202205.0027.v1

model, resulting in an overall rise in temperature. Due to conduction, heat from the first few beads were dissipated in the tool, and its temperature was increased. As the tool was reheated with multiple beads, the overall temperature of the model began to rise, and the only medium of cooling was direct cooling by air. The reheating caused the 5-bead model to cool slowly, and the beads induced less compressive stresses on the tool than 2-beads. Therefore, for the same-sized beads, the compressive stresses induced on the tool surface by the 2-beads model were greater than that caused by the 5-beads model. As a result, the tool with fewer beads appeared more robust than the tool with more beads, as also stated by Z. Hu et al. [78]. In the case of steel 309L, the maximum compressive stress of σ_m = -128 MPa was generated by 2-beads with dimensions A4.

3.3.2. Influence of a gap between the beads

As previously noted, most of the compressive stresses on the tool surface were located directly underneath the weld beads. The number of beads in weld cladding also affects the compressive stresses induced on the tool. The maximum compressive stresses on the tool decrease as the number of parallel beads increase (see section 3.3.1). In the multiple beads model, the reheating limits the maximum achievable compressive stresses of the individual bead. The reheating causes the conversion of the compressive stresses back into tensile stresses. With the 100 mm diameter tool and beads of dimension A3 (w = 6 mm, h = 4 mm), the smallest or critical gap necessary to minimize the reheating effect in multiple parallel beads is determined in Figure 20.

If there is no or a small gap (up to 11 mm) between the two parallel beads, the maximum compressive stresses generated on the tool surface by the first bead are less than that of the second bead. As the distance between the two parallel beads increases, the compressive stress on the tool by the first bead increases. After a critical gap of 11 mm between the adjacent beads, their effect on each other becomes almost negligible. The maximum compressive stress generated by both the beads becomes the same. The maximum compressive stress on the tool remains unchanged as the distance between the beads is increased further.

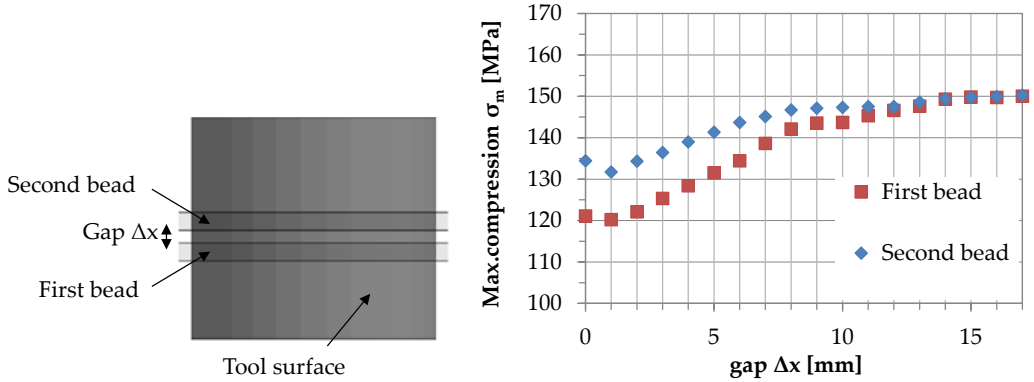

Figure 20. Influence of a gap between the two consecutive parallel weld beads (dimensions A3) on the maximum compressive stresses induced on the 100 mm diameter tool after cooling.

If the distance between the two beads is above 15 mm, there is no influence of the temperature on the compressive stress generated by each of the beads. It can be inferred that the minimum gap between the two parallel weld beads should be equal to the critical gap of 11 mm to maximize the resultant compressive stresses on the tool surface.

3.3.3. Influence of the internal hole in the tool

In this sub-section, the tools with a tapered hole along the length of the cylinder have been considered. The stiffness of the tool is weakened in the cross-section as the hole becomes larger. Thus, with a large diameter hole, the tool can deform elastically, and the reinforcement effect due to shrinkage of the weld beads is reduced. Five models were simulated

Preprints (www.preprints.org) | NOT PEER-REVIEWED | Posted: 5 May 2022 doi:10.20944/preprints202205.0027.v1

with the beads welded on the tool at different positions (see Figure 5, Figure 21 (a)). It is to be noted here that only one bead is welded at one of the five positions in one model. The maximum compressive stress produced by a bead welded at various positions on the tool surface is depicted in Figure 21 (b). In contrast, the stresses inside the tool are shown in Figure 22.

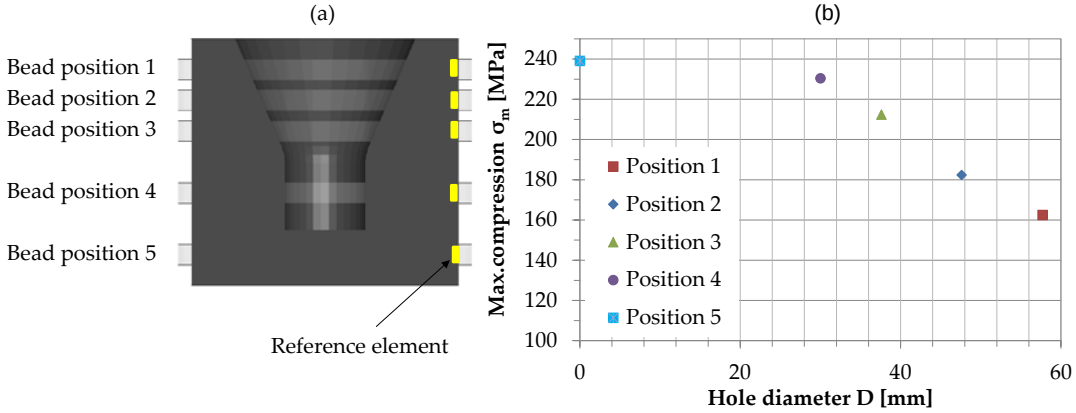

Figure 21. Different positions of a single bead on the tool surface (one bead in one numerical model) (a) and Influence of inner hole diameter D on the maximum compressive stresses on the tool's surface (b).

At position 1, where the tool has an inner hole diameter of 57.7 mm underneath the bead, developed the maximum compressive stress of $\sigma_{m,\,max}$ = 162 MPa. The maximum compressive stress increased from $\sigma_{m,\,max}$ = 182.45 MPa to $\sigma_{m,\,max}$ = 230.47 MPa as the hole diameter reduced, i.e., from position 2 to position 4. The maximum compressive stress has been achieved on the tool with a bead at position 5 and accounts for approximately $\sigma_{m,\,max}$ = 239.1 MPa. Therefore, it can be concluded that the hole diameter and the maximum compressive on the tool surface are inversely proportional to each other. The bead's position on the tool without a hole underneath resulted in more compressive stress; therefore, more reinforcement can be achieved there on the tool after cooling.

In each of the models with different bead positions, the stress distribution in the tool after cooling and unclamping can be seen in Figure 22. Analogous to the increase in stiffness in the tool, an increase in compressive stress is also visible in the cross-section of the tool underneath the bead. The difference in the stress distribution on the left and right sides of the part is just due to the start and endpoint of the trajectory. The compressive region was smaller in models 1 and 2 because the hole diameter under the bead was bigger. As the hole diameter decreased, more compressive stress was induced on the tool surface (under the bead), and more tensile stress was produced within the tool to balance it, as shown in models 3 and 4. The bead position in model 5 caused more compressive stress on the tool surface, which is visible as a wider blue region on the surface.

Preprints (www.preprints.org) | NOT PEER-REVIEWED | Posted: 5 May 2022 doi:10.20944/preprints202205.0027.v1

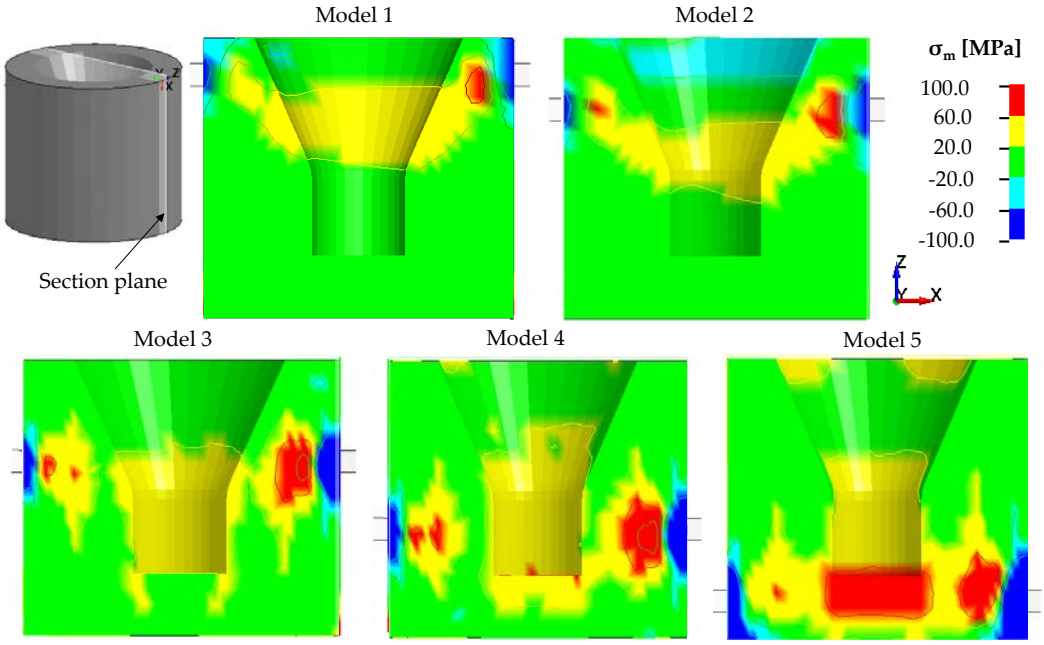

Figure 22. Distribution of the compressive and tensile stresses in the tool (along the cross-section).

The beads welded at positions 1 and 2 resulted in rapid cooling through conduction and convection, resulting in a smaller tensile region in the middle of the tool. As the hole diameter reduced, cooling became slower, and a larger tensile area emerged inside the tool, as shown in models 3 and 4. In the case of model 5, most of the heat exchange was carried out by convection with the external surface of the tool, as there was no hole under the bead. Therefore, a wider compressive region appeared along the surface.

3.3.4. Influence of a time delay between the weld-beads

The addition of pause time or delay between the weld beads can influence the compressive stress state on the tool surface after cooling. A time delay of 20 s was kept before welding the next bead until all the beads were welded. A comparison of the stress histories of the tool elements in two parallel-bead models with and without time delay is shown in Figure 23. The addition of a time delay of up to 20s in the 2-beads model has not shown any noticeable difference. However, the delay resulted in relatively less compressive stresses on the tool surface in the 5-beads model. Compared to the model without delay, the tool cooled more and was reheated to a lower peak during the welding of the next bead. Hence, the beads in the model, without delay, on cooling, shrunk more and generated more compressive stresses on the tool. The model cooled more quickly as a result of the delay. Hence, the heat did not accumulate, and comparatively less shrinkage was observed on cooling, as also described by Lanxess [77]. The continuous welding of the 5-beads without delay induced approximately 5-15 MPa more compressive stresses on the referenced element than the model with delay and minimized substrate distortion, as reported by M.P. Mughal et al. [79]. The delay between the weld beads only increases production time and decreases the reinforcement. Therefore, fewer beads and welding strategies without time delay are preferred.

Preprints (www.preprints.org) | NOT PEER-REVIEWED | Posted: 5 May 2022 doi:10.20944/preprints202205.0027.v1

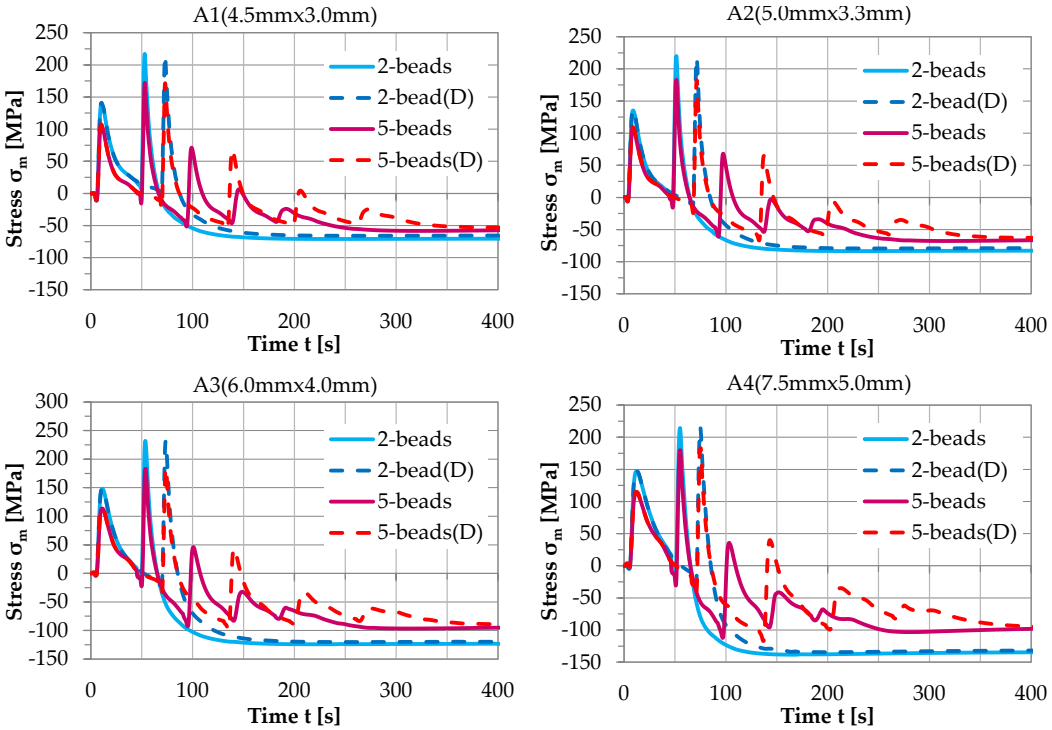

Figure 23. Comparison of stress history of the tool elements with 2 and 5 parallel beads of dimensions (A1-A4), welded with delay (D = 20 s) and without time delay between the beads.

3.3.5. Influence of the welding direction

The direction of the adjacent bead was reversed to investigate the influence of welding direction on induced compressive stresses, as shown in Figure 24. The thermo-mechanical history of the model with the reversed welding direction (R) was found to be different from that of the model with the same-direction welding. However, because input energy and welding time were the same in both models, comparable compressive stresses on the tool after cooling were observed. Again, the same relation was found: 2-beads developed more compressive stress on the toll than 5-beads, and bigger beads compressed the tool more than smaller beads.

Preprints (www.preprints.org) | NOT PEER-REVIEWED | Posted: 5 May 2022 doi:10.20944/preprints202205.0027.v1

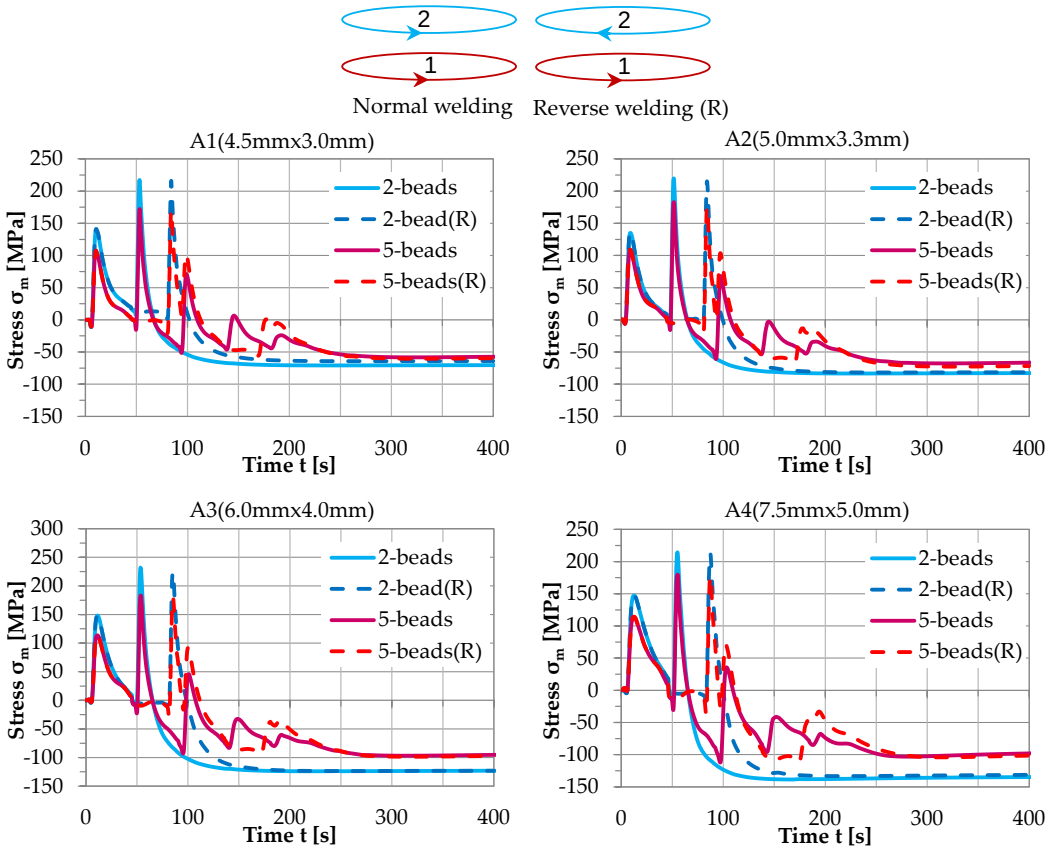

Figure 24. Comparison of stress history of the tool-elements with 2 and 5 parallel beads of dimensions (A1-A4), welded in normal and reversed welding direction (R).

3.4. Optimization of the multiple-layered weld-cladding patterns

Tool reinforcement improves load-bearing capacity and protects operators from unexpected tool failure. This section concerns thick or multiple layered weld beads. Following the previous findings, the two parallel beads welded individually in a single layer induced more tool compressive stresses than the five parallel beads. Therefore, in this section, only two parallel beads will be tested in multiple layers (two and three layers), and their outcomes will be compared and optimized to enhance the compressive stresses in the tool. In the latter text following acronyms will be used:

- 2x1 = A single layer of 2 beads welded parallel to each other
- 2x2 = Two welding layers, each layer having two parallel beads
- 2x3 = Three welding layers, each layer having two parallel beads

The 2x1 pattern has already been discussed in Section 2.2.1. A schematic illustration of the 2x2 and the 2x3 pattern is shown in Figure 8.

3.4.1. Influence of different trajectories

As described in section 3.3.5, the thermal history of the weld-cladding process depends on the welding trajectory. In this section, different welding trajectories (T1-T5) (see Figure 10) in the 2x2 pattern were compared to determine the best welding trajectory to generate the maximum compressive stress in the tool. A comprehensive comparison of the stress histories of the aforementioned trajectories welded with beads of different dimensions, i.e., A1-A4, is shown in Figure 25.

Preprints (www.preprints.org) | NOT PEER-REVIEWED | Posted: 5 May 2022 doi:10.20944/preprints202205.0027.v1

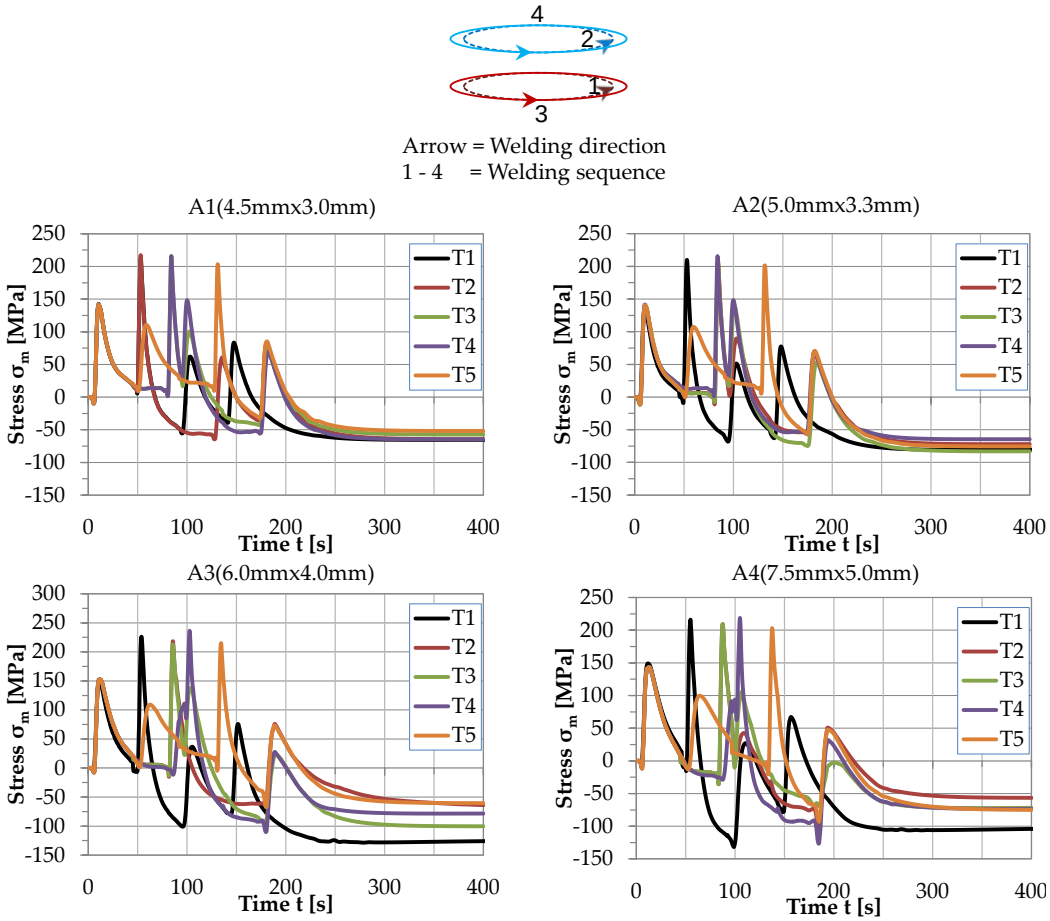

Figure 25. Comparison of the stress history of the tool-element for different welding trajectories in a 2x2 pattern with beads of dimensions (A1-A4).

Among all the trajectories T1-T5, the trajectory T1 induced the maximum compressive stress on the tool. The maximum compressive stress of $\sigma_{m,\,max}$ = -113 MPa, has been induced on the tool using A4 beads. Trajectory T2 also appeared to be a good trajectory with cross-sections A1 and A2 (see Figure 25). With beads ranging in size from A1 to A3, the trajectory T4 produced maximum compressive stress of about $\sigma_{m,\,max}$ = -108 MPa with A3 beads. T1 is regarded as a better and more optimal trajectory than the other trajectories, since the beads in this trajectory generated the most considerable compressive stresses on the tool after cooling

3.4.2. Influence of adding multiple layers

A thick layer of reinforcement in a 2x3 (three-layer) pattern has been simulated using trajectory T1 to avoid tool breakage owing to overload. A detailed comparison of two parallel beads in one, two, and three layers is shown in Figure 26.

Preprints (www.preprints.org) | NOT PEER-REVIEWED | Posted: 5 May 2022 doi:10.20944/preprints202205.0027.v1

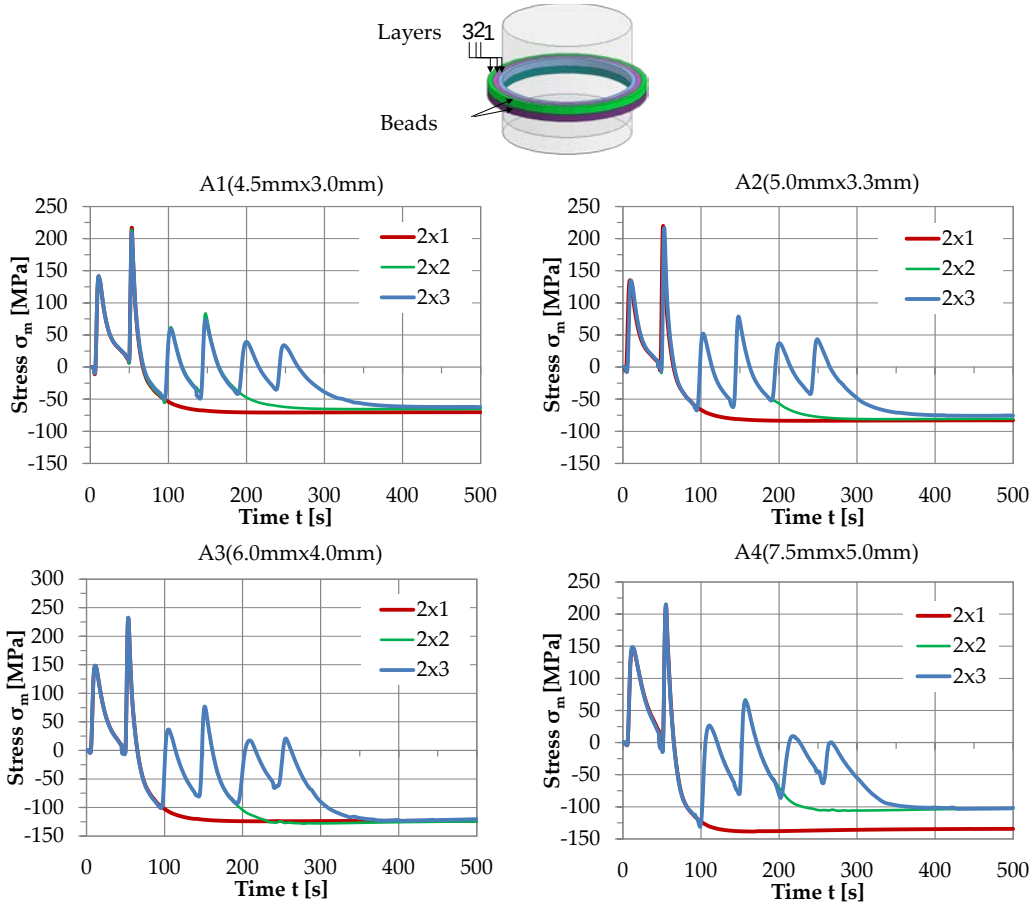

Figure 26. Comparison of the stress history of the tool-element in multiple layers welding with A1-A4 beads.

It can be noticed that the beads in a single layer (2x1 pattern) developed the maximum compressive stress on the tool surface. The maximum compressive stress in the tool was generated by the larger beads (A4) with its maximum value as $\sigma_{m,\,max}$ = -128 MPa. The A4 -beads developed less compressive stresses in the tool with a 2x3 pattern than the 2x2 or 2x1 pattern. The reheating of the layers added more heat to the tool, resulting in slow cooling and variations in the microstructure and mechanical properties. Consequently, the beads do not shrink as much as laid down in a single layer.

3.5. Maximum compressive stresses in different practical scenarios

3.5.1. Reinforcement of the tool under operating conditions

The behavior of the extrusion tool reinforced by the weld-cladding process and conventional method is examined at different temperatures achieved during extrusion to evaluate the effect of extreme conditions on the tool's reinforcement. The reinforced tools are heated to higher temperatures, i.e., from 25 °C to 800 °C, corresponding to the operating temperatures during extrusion. After cooling from various operating temperatures, the compressive stresses (reinforcement) on the tool surface (under the bead) were reduced. Compressive stress decreased following the same pattern in weld-cladding and conventional processes. During the weld-cladding process, the reinforcement on the extrusion tool declines at a rate of 8 % for every 100 °C increase in temperature from 25 °C to 400 °C. At higher working temperatures from 400 °C to 700 °C, the tool's reinforcement deteriorated at a rate of about 40 %. At 800 °C, the tool's reinforcement decreased to approximately 98 % of its starting value, reaching just 4 MPa after cooling. In contrast to the weld-cladding process, the tool reinforced by the conventional method lost its strength rapidly up to 500 °C. As operating temperatures climb from 600 °C to 800 °C, the decline in tool

Preprints (www.preprints.org) | NOT PEER-REVIEWED | Posted: 5 May 2022 doi:10.20944/preprints202205.0027.v1

reinforcement with temperature becomes the same with both methods, as shown in Figure 27.

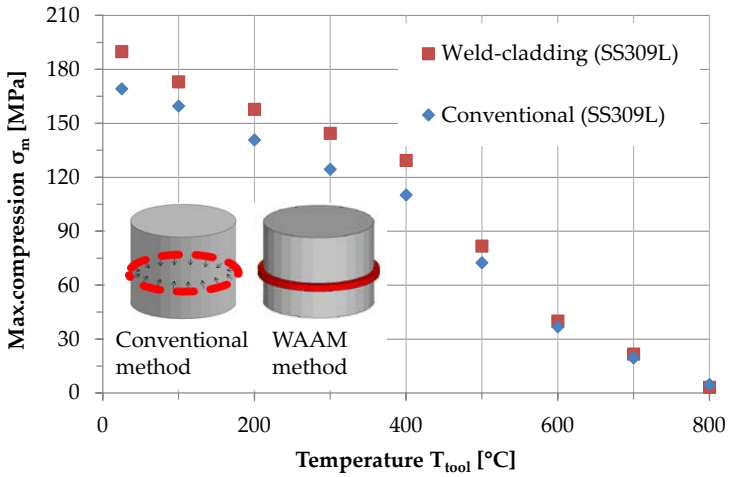

Figure 27. Maximum compressive stresses (reinforcement) on the tool surface, achieved at different operating conditions of the extrusion tool.

Since the same material was used for the computational analysis of weld-cladding and conventional methods, a similar trend was observed under different operating conditions. As a result, it may be anticipated that the material's thermo-mechanical properties significantly impact the reinforcement. Hence, weld-cladding can be employed as a low-cost alternative to more expensive traditional procedures for providing enough reinforcement on the components.

3.5.2. Influence of the tool's diameter on the maximum compressive stresses under different operating conditions

Weld cladding on several tool diameters, i.e., 40 mm, 45 mm, 50 mm, 55 mm, 60 mm, and 65 mm (see Figure 6), was numerically tested to determine if the tool diameter changes the compressive stresses on the tool surface. The width and height for each bead were kept constant, i.e., 8 mm and 5 mm, while the inner diameter of the beads was adjusted to fit the outer diameter of the tool. Simulations were carried out at three different operating conditions as mentioned:

i) Constant velocity: The welding velocity and heat input remained unchanged, while the welding time was adjusted based on the length of the welding path.
ii) Constant welding time: The welding time was constant, while the welding velocity and heat input were adjusted based on the cross-sectional area of the weld-bead.
iii) Maximal reinforcement: The entire bead was heated beyond the melting point and then cooled to room temperature using the efficient method.

In the first case, as the tool's diameter increases, so does the volume and the welding path; thus, extra welding time is required to weld the bead. In the second case, the effect of a larger diameter is compensated for by changing the welding velocity and power. The total heat input on a unit volume remains constant while maintaining the welding time. The third case considers an efficient situation in which local heating and cooling effects are eliminated by heating the bead above the melting temperature, i.e., 1700 °C, followed by air cooling to room temperature.

The average of maximum-compressive stresses of all the tool's elements under the bead at different operating conditions is shown in Figure 28.

Preprints (www.preprints.org) | NOT PEER-REVIEWED | Posted: 5 May 2022 doi:10.20944/preprints202205.0027.v1

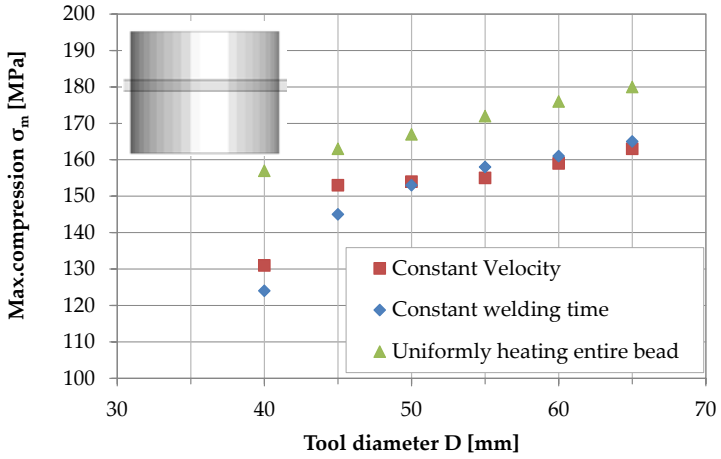

Figure 28. Maximum compressive stresses induced by a bead on the tool surface having different diameters at different operating conditions.

The heat loss to the air intensified as the tool's diameter increased. The compressive stress developed by the bead on the smaller diameter tool was less than the larger tools in all cases. When the tool diameter increased, so did the length of the weld-bead and its subsequent heat input, resulting in enhanced compressive stress on the tool surface after cooling. When the tool diameter exceeds 50 mm, the curves of cases 1 and 2 become nearly identical. Since the behavior of compressive stresses with increasing tool diameter is consistent in all situations, it also confirms the validity of the weld-cladding approach used in this work.

3.5.3. Influence of heat source velocity on maximum compressive stresses

Different welding velocities have been tested using the standard weld-cladding numerical procedure and material properties of steel 309L. The dimensions of the tool and the bead were kept consistent for all models. The heat input in all the models was kept the same by keeping a constant ratio between the input energy and the heat-source velocity. After welding, the models were allowed to cool for the next 400 s before being analyzed. The following heat source velocities were tested i.e. 7.5 mm/s, 15 mm/s, 20 mm/s, 25 mm/s, 30 mm/s and 35 mm/s. The average of the maximum compressive stresses on all the elements of the tool surface under the bead at different heat-source velocities is shown in Figure 29.

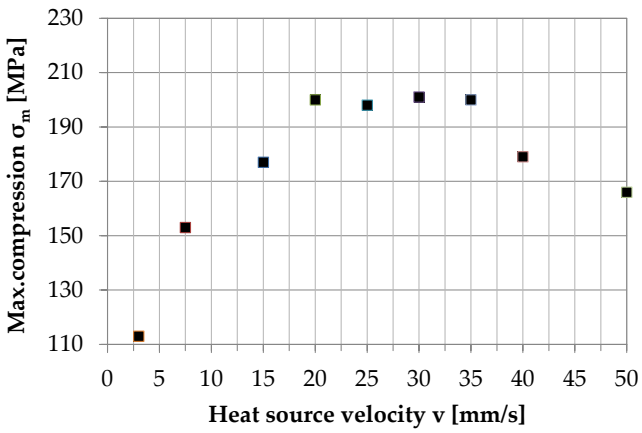

Figure 29. Comparison of the average of the maximum compressive stresses of all the elements of the tool surface under the bead at different heat source velocities.

As the heat source travel speed increased, the maximum compressive stresses on the tool surface increased up to a velocity of 20 mm/s, where the maximum compressive stress of

 doi:10.20944/preprints202205.0027.v1

$\sigma_{m,max}$ = 201 MPa was reached. With the further increase in heat source travel speed, the maximum compressive stresses on the tool surface remained almost unchanged up to 35 mm/s. Due to insufficient heating of the bead and tool, the compressive stresses in the tool decreased as the heat source travel speed increased beyond 35 mm/s. Hence, the optimal velocity range for welding the tool with the given dimensions is between 20 and 35 mm/s.

4. **Summary and Conclusions**

In the present research, a novel approach aiming at utilizing the weld-cladding process to targetly generate desired compressive residual stresses is presented at the example of a demonstrator tool. During welding, thermal expansion and contraction of weld beads have been effectively used to develop compressive stresses near the tool's surface. The experimental results validated the temperature distribution and residual stresses of the numerical investigations. Simulations with various welding and geometrical parameters such as continuous welding (with and without delay) and welding in different trajectories were performed to obtain the optimized process parameters and path for tool reinforcement. A comparison of weld-cladding and conventional methods was performed to validate the efficiency of the weld-cladding in various practical scenarios.

The conclusions and suggestions that can be drawn from this work are as follows:

- Approximately 40 – 60 % residual stresses in the tool surface are induced by mechanical contact of beads to the tool, while the rest developed due to repeated thermal cycles.
- The thermal contraction of the weld bead and the thermal expansion and contraction of the tool during the wire-arc welding process can be used to strengthen the tools.
- Repeated heating and cooling of beads accumulate heat within the model, resulting in slow cooling and reduced tool reinforcement.
- In the multiple bead welding process, reheating reduces the compressive stresses generated by the previous beads on the tool. With the 100 mm diameter of a tool, and beads of dimension A3 (h = 4 mm, w = 6 mm), establishing a minimum gap $\Delta x \geq 11$ mm reduces the thermal influence of the adjacent beads.
- During welding, the weld bead with a larger cross-section should be preferred. The beads of dimension A4 (7.5 mm x 5 mm) introduced the maximum compressive stresses in the tool in almost all the welding patterns. Therefore, they can be adapted to reinforce the components more effectively.
- The weld-cladding of multiple beads (5-beads) in parallel sequence without delay adds more reinforcement to the tool and minimizes distortion compared to the welding with a time delay between each bead.
- Due to heat accumulation, adding each new layer in a multilayer weld-cladding process mitigates the compressive stresses in the tool. For example, when welding the tool with A4 beads, the 2-layered (2 x 2) pattern produced approximately 11 - 14 % less compressive stresses than the 1-layered (2 x 1) pattern. Similarly, the 3-layered (2 x 3) pattern induced even less compressive stresses in the tool.
- The tool's reinforcement is reduced to 98 % of its initial value during an extrusion operation at an operating temperature of 800 °C.
- Internal features like a hole or a notch reduce the tool's stiffness.
- Increasing the tool and bead diameters improves heat flow and increases the maximum compressive stresses on the tool surface after cooling.

Based on the investigated rules, an optimized weld-cladding approach with better parameters can be designed to achieve low-cost reinforcement of different components. Overall, reinforcement of tooling by weld-cladding could be a low-cost alternative that incorporates considerable compressive stresses with a single weld bead or thin layer. If thick reinforcements are required, multiple layers should be welded together.

Author Contributions: Conceptualization and methodology, Markus Bambach, Johannes Buhl and Rameez Israr.; software, Rameez Israr; Investigation and validation, Rameez Israr and Johannes Buhl; writing—original draft preparation, Rameez Israr; writing—review and editing, Rameez Israr, Johannes Buhl, Markus Bambach and Sebastian Härtel; Supervision, Johannes Buhl, Markus Bambach. All authors have read and agreed to the published version of the manuscript.

Funding: This research was funded by the European Union from the European Regional Development Fund (EFRE), grant number 85037495.

Data Availability Statement: Not applicable.

Acknowledgments: The research project EFRE 85037495 "MALEDIF - Maschinelles Lernen für die additive Fertigung" was supported by the European Union from the European Regional Development Fund (EFRE). The project was carried out at the Department of Hybride Manufacturing. The authors would like to thank Mr. Lam for helping out in a part of the experimental investigations.

Conflicts of Interest: The authors declare no conflict of interest. The funders had no role in the design of the study; in the collection, analyses, or interpretation of data; in the writing of the manuscript, or in the decision to publish the results.

5. References

[1] Bambach M, Sviridov A, Weisheit A, Schleifenbaum J. Case Studies on Local Reinforcement of Sheet Metal Components by Laser Additive Manufacturing. Metals 2017;7(4):113.

[2] Teller M, Bambach M, Hirt G, Ross I, Temmler A, Poprawe R et al. Investigation of the Suitability of Surface Treatments for Dry Cold Extrusion by Process-Oriented Tribological Testing. KEM 2015;651-653:473–9.

[3] Hope MJ, Bally MB, Webb G, Cullis PR. Production of large unilamellar vesicles by a rapid extrusion procedure. Characterization of size distribution, trapped volume and ability to maintain a membrane potential. Biochimica et Biophysica Acta (BBA) - Biomembranes 1985;812(1):55–65.

[4] Namburi KPV, Kothasiri AF, Yerubandi VSM. Modeling and simulation of Aluminum 1100 alloy in an extrusion process. Materials Today: Proceedings 2019.

[5] Schrader T, Shirgaokar M, Altan T. A critical evaluation of the double cup extrusion test for selection of cold forging lubricants. Journal of Materials Processing Technology 2007;189(1-3):36–44.

[6] Lee HY, Noh JH, Hwang BB. Surface stresses and flow modes on contact surface in a combined double cup extrusion process. Tribology International 2013;64:215–24.

[7] Zare HR, Darijani H. A novel autofrettage method for strengthening and design of thick-walled cylinders. Materials & Design 2016;105:366–74.

[8] Arbak M. Material adapted design of cold forging tools exemplified by powder metallurgical tool steels and ceramics. Zugl.: Erlangen-Nürnberg, Univ., Diss., 2012. Bamberg: Meisenbach; 2012.

[9] Klocke F. Manufacturing Processes 4. Berlin, Heidelberg: Springer Berlin Heidelberg; 2013.

[10] Lange K. Massivumformung. 2nd ed. Berlin: Springer; 1988.

[11] Tzeng JT, Moy P. Composite Energy Storage Flywheel Design for Fatigue Crack Resistance. IEEE Trans. Magn. 2009;45(1):480–4.

[12] Haneklaus N, Reuven R, Cionea C, Hosemann P, Peterson PF. Tube expansion and diffusion bonding of 316L stainless steel tube-to-tube sheet joints using a commercial roller tube expander. Journal of Materials Processing Technology 2016;234:27–32.

[13] Rees DWA. THE FATIGUE LIFE OF THICK-WALLED AUTOFRETTAGED CYLINDERS WITH CLOSED ENDS. Fat Frac Eng Mat Struct 1991;14(1):51–68.

[14] Kanber B. Boundary Element Analysis of Interference Fits 2006;30.

[15] ASI. American National Standard Preferred Hole Basis Metric Clearance Fits; 1978 (R2004); Available from: http://www.zpag.net/Usinage/standard_ansiB4_2_1978.htm.

[16] SCHAEFFLER. Mounting and Dismounting of Rolling Bearings.

[17] A M, S JJ, P BA. Fatigue analysis of thermal shrink-fit autofrettage in pressure cylinder using finite element analysis. Journal of Materials Research and Technology 2020;9(4):8606–17.

[18] Mather J, Baines BH. Distribution of stress in axially symmetrical shrink-fit assemblies. Wear 1972;21(2):339–60.

[19] DriscoPlex. Engineering Considerations for Temperature Change. [July 17, 2019]; Available from: http://www.performancepipe.com/en-us/Documents/PP814-TN%20Thermal%20Effects.pdf.

[20] Abdelsalam OR. Design optimization for a three-layers shrink-fitted pressure vessel exposed to very high pressure. IOP Conf. Ser.: Mater. Sci. Eng. 2019;610:12077.

[21] Armanios EA, Bucinell RB, Wilson DW, Tzeng JT. Viscoelastic Modeling of Press-Fitted Composite Cylinders. J. Compos. Technol. Res. 2001;23(1):21.

[22] Beghini M, Loffredo M, Monelli BD, Bagattini A. Residual stress measurements in an autofrettaged cylinder through the Initial Strain Distribution method. International Journal of Pressure Vessels and Piping 2018;168:87–93.

[23] Thumser R, Bergmann JW, Vormwald M. Residual stress fields and fatigue analysis of autofrettaged parts. International Journal of Pressure Vessels and Piping 2002;79(2):113–7.

[24] Haghpanah Jahromi B, Farrahi GH, Maleki M, Nayeb-Hashemi H, Vaziri A. Residual stresses in autofrettaged vessel made of functionally graded material. Engineering Structures 2009;31(12):2930–5.

[25] Shufen R, Dixit US. An analysis of thermal autofrettage process with heat treatment. International Journal of Mechanical Sciences 2018;144:134–45.

[26] Kamal SM, Borsaikia AC, Dixit US. Experimental assessment of residual stresses induced by the thermal autofrettage of thick-walled cylinders. The Journal of Strain Analysis for Engineering Design 2016;51(2):144–60.

[27] Malik MA, Rashid B, Khan M, Khushnood S. Modeling and Simulation of Residual Stresses in Mechanical Autofrettage. In: ASME 2005 International Mechanical Engineering Congress and Exposition; 2005, p. 905–913.

[28] Kaplan M, Glick H, Howell W, D'Souza V. The Radial Piston Approach to the Explosive Autofrettage of Thickwalled Forging Dies. In: Tobias SA, Koenigsberger F, editors. Proceedings of the Thirteenth International Machine Tool Design and Research Conference. London: Macmillan Education UK; 1973, p. 419–426.

[29] Zare HR, Darijani H. Strengthening and design of the linear hardening thick-walled cylinders using the new method of rotational autofrettage. International Journal of Mechanical Sciences 2017;124-125:1–8.

[30] Perl M, Saley T. The detrimental effect of autofrettage on externally cracked modern tank gun barrels. Defence Technology 2019;15(2):146–53.

[31] Gavriljuk VG, Berns H, Escher C, Glavatskaya NI, Sozinov A, Petrov YN. Grain boundary strengthening in austenitic nitrogen steels. Materials Science and Engineering: A 1999;271(1-2):14–21.

[32] Cáceres CH, Rovera DM. Solid solution strengthening in concentrated Mg–Al alloys. Journal of Light Metals 2001;1(3):151–6.

[33] Morita T, Hatsuoka K, Iizuka T, Kawasaki K. Strengthening of Ti–6Al–4V Alloy by Short-Time Duplex Heat Treatment. Mater. Trans. 2005;46(7):1681–6.

[34] Gladman T. Precipitation hardening in metals. Materials Science and Technology 2013;15(1):30–6.

[35] Zehetbauer M, Seumer V. Cold work hardening in stages IV and V of F.C.C. metals—I. Experiments and interpretation. Acta Metallurgica et Materialia 1993;41(2):577–88.

[36] Venkateswara Rao N, Madhusudhan Reddy G, Nagarjuna S. Weld overlay cladding of high strength low alloy steel with austenitic stainless steel – Structure and properties. Materials & Design 2011;32(4):2496–506.

[37] Lamet et al. Welding, brazing and soldering: ASM Handbook. 9th ed. OH, USA; 1983.

[38] Pan Y-m, Chen S-w. Research on overlaying welding rod of high hardness maraging steel. Front. Mech. Eng. China 2006;1(4):465–7.

 doi:10.20944/preprints202205.0027.v1

[39] Jiang WC, Wang BY, Gong JM, Tu ST. Finite element analysis of the effect of welding heat input and layer number on residual stress in repair welds for a stainless steel clad plate. Materials & Design 2011;32(5):2851–7.

[40] Benghalia G, Wood J. Autofrettage of Weld Clad Components. Procedia Engineering 2015;130:453–65.

[41] Schnier G, Wood J, Galloway A. Investigating the Effects of Process Variables on the Residual Stresses of Weld and Laser Cladding. AMR 2014;996:481–7.

[42] Luo F, Yao J-h, Hu X-x, Chai G-z. Effect of Laser Power on the Cladding Temperature Field and the Heat Affected Zone. J. Iron Steel Res. Int. 2011;18(1):73–8.

[43] Gao W, Zhao S, Wang Y, Zhang Z, Liu F, Lin X. Numerical simulation of thermal field and Fe-based coating doped Ti. International Journal of Heat and Mass Transfer 2016;92:83–90.

[44] Kumar A, Roy S. Effect of three-dimensional melt pool convection on process characteristics during laser cladding. Computational Materials Science 2009;46(2):495–506.

[45] Smith MC, Smith AC, Wimpory R, Ohms C. A review of the NeT Task Group 1 residual stress measurement and analysis round robin on a single weld bead-on-plate specimen. International Journal of Pressure Vessels and Piping 2014;120-121:93–140.

[46] Karlsson L, Goldak J. Computational Welding Mechanics. In: Hetnarski RB, editor. Encyclopedia of Thermal Stresses. Dordrecht: Springer Netherlands; 2014, p. 630–637.

[47] Lindgren L-E. Modelling options in computational welding mechanics (CWM). In: Computational Welding Mechanics. Elsevier; 2007, p. 119–163.

[48] Foroozmehr E, Kovacevic R. Effect of path planning on the laser powder deposition process: thermal and structural evaluation. Int J Adv Manuf Technol 2010;51(5-8):659–69.

[49] R. Israr, J. Buhl, L. Elze, M. Bambach (ed.). Simulation of different path strategies for wire-arc additive manufacturing with Lagrangian finite element methods. Cottbus: Israr, Rameez; 2018.

[50] Boyer R. Materials properties handbook: titanium alloys. ASM International: ASM International; 1994.

[51] Hurly JJ. Thermophysical Properties of Gaseous CF4 and C2F6 from Speed-of-Sound Measurements. Int J Thermophys 1999;20(2):455–84.

[52] Markus kind TB. Ti6Al4V/Titan Grade 5/3.7164. Köln; Available from: http://www.kind-aerospace.de/pdf/Werkstoffdatenblatt_120402.pdf. [September 16, 2020].

[53] Chen H-C, Pinkerton AJ, Li L. Fibre laser welding of dissimilar alloys of Ti-6Al-4V and Inconel 718 for aerospace applications. Int J Adv Manuf Technol 2011;52(9-12):977–87.

[54] Vday Additive manufacturing Technology Co.Ltd. Inconel 718. [October 05, 2020]; Available from: https://search.totalmateria.com/MaterialDetails/MaterialDetail?vkKey=3302429&keyNum=5&type=1&hs=0.

[55] Nadimi S, Khoushehmehr RJ, Rohani B, Mostafapour A. Investigation and Analysis of Weld Induced Residual Stresses in Two Dissimilar Pipes by Finite Element Modeling. J. of Applied Sciences 2008;8(6):1014–20.

[56] Guanyu Tube. 304L Physical Properties. [September 16, 2020]; Available from: https://tubingchina.com/304L-Physical-Property.htm.

[57] SONMEZ U, CEYHUN V. Investigation of mechanical and microstructural properties S 235 JR (ST 37-2) steels welded joints with FCAW. km 2016;52(01):57–63.

[58] MakeItFrom. EN 1.0038 (S235JR) Non-Alloy Steel. [September 16, 2020]; Available from: https://www.makeitfrom.com/material-properties/EN-1.0038-S235JR-Non-Alloy-Steel.

[59] Jeyakumar M, Christopher T. Influence of residual stresses on failure pressure of cylindrical pressure vessels. Chinese Journal of Aeronautics 2013;26(6):1415–21.

 doi:10.20944/preprints202205.0027.v1

[60] Steel Grades. ASTM A36. [September 16, 2020]; Available from: https://www.steel-grades.com/Steel-Grades/Carbon-Steel/ASTM-A36.html.

[61] Wadsworth J, Nieh TG, Stephens JJ. Recent advances in aerospace refractory metal alloys. int. mat. rev. 1988;33(1):131–50.

[62] Portelli M, Bertarelli A, Carra F, Pasquali M, Sammut N, Mollicone P. Numerical and experimental benchmarking of the dynamic response of SiC and TZM specimens in the MultiMat experiment. Mechanics of Materials 2019;138:103169.

[63] Harris. Technical Specification Sheet 309L Stainless Steel Welding Wire. [September 24, 2020].

[64] Ebrahimi A, Mohammadi M. Numerical tools to investigate mechanical and fatigue properties of additively manufactured MS1-H13 hybrid steels. Additive Manufacturing 2018;23:381–93.

[65] Kerfriden P, Claus S, Mihai I. A mixed-dimensional CutFEM methodology for the simulation of fibre-reinforced composites. Adv. Model. and Simul. in Eng. Sci. 2020;7(1).

[66] Simufact. Info-Sheet Heat source. [June 20, 2019]; Available from: https://studylib.net/doc/8338133/info-sheet-heat-source.

[67] Goldak J, Chakravarti A, Bibby M. A new finite element model for welding heat sources. MTB 1984;15(2):299–305.

[68] ISRAR R, Buhl J, Bambach M. Numerical Analysis of Different Fixation Strategies in Direct Energy Deposition Processes. Procedia Manufacturing 2020;47:1184–9.

[69] Teng T-L, Chang P-H, Tseng W-C. Effect of welding sequences on residual stresses. Computers & Structures 2003;81(5):273–86.

[70] American Welding Society. Specification for Carbon Steel Electrodes and Rods for Gas Shielded Arc Welding(ANSI/AWS A5.18-93). Florida: American welding society; 1993; Available from: http://www.esfahanfoolad.com/UserImages/file/Standards/101.pdf. [August 28, 2019].

[71] Deutsches Institut für Normung DIN. Material specification sheet(DIN-EN-10025-2); Available from: http://www.steelss.com/Carbon-steel/s235.html. [October 21, 2019].

[72] Ge J, Lin J, Lei Y, Fu H. Location-related thermal history, microstructure, and mechanical properties of arc additively manufactured 2Cr13 steel using cold metal transfer welding. Materials Science and Engineering: A 2018;715:144–53.

[73] Nguyen L, Buhl J, Bambach M. Continuous Eulerian tool path strategies for wire-arc additive manufacturing of rib-web structures with machine-learning-based adaptive void filling. Additive Manufacturing 2020;35:101265.

[74] Yadaiah N, Bag S. Effect of Heat Source Parameters in Thermal and Mechanical Analysis of Linear GTA Welding Process. ISIJ Int. 2012;52(11):2069–75.

[75] LS-DYNA Support. Equation of state. [March 06, 2020]; Available from: https://www.dynasupport.com/howtos/general/equation-of-state.

[76] Jousten K, Hendricks J, Barker D, Douglas K, Eckel S, Egan P et al. Perspectives for a new realization of the pascal by optical methods. Metrologia 2017;54(6):S146-S161.

[77] Lanxess. Shrinkage and distortion calculation. [July 05, 2019]; Available from: https://techcenter.lanxess.com/scp/americas/en/techServscp/79017/article.jsp?print=true&docId=79015.

[78] Hu Z, Qin X, Shao T. Welding Thermal Simulation and Metallurgical Characteristics Analysis in WAAM for 5CrNiMo Hot Forging Die Remanufacturing. Procedia Engineering 2017;207:2203–8.

[79] Mughal MP, Fawad H, Mufti R. Finite element prediction of thermal stresses and deformations in layered manufacturing of metallic parts. Acta Mechanica 2006;183(1-2):61–79.